Physica E 76 (2016) 12–27

Contents lists available at ScienceDirect

Physica E

journal homepage: www.elsevier.com/locate/physe

Time dependent electronic transport in chiral edge channels

G. Fève *, J.-M. Berroir, B. Plaçais

Laboratoire Pierre Aigrain, Ecole Normale Supérieure-PSL Research University, CNRS, Université Pierre et Marie Curie-Sorbonne Universités, Université Paris Diderot-Sorbonne Paris Cité, 24 rue Lhomond, 75231 Paris Cedex 05, France

HIGHLIGHTS

- We discuss Coulomb interaction effects on charge propagation along quantum Hall edge channels.
- Various experimental works are connected and analyzed in a unified theoretical framework.
- Low frequency transport is described by a lumped element model.
- High frequency transport is described by edge magnetoplasmon propagation.
- Interchannel magnetoplasmon scattering leads to electron fractionalization and decoherence.

ARTICLE INFO

Article history:
Received 1 July 2015
Received in revised form
1 October 2015
Accepted 3 October 2015
Available online 9 October 2015

Keywords:
Quantum Hall effect
Time dependent transport
Mesoscopic capacitor
Fractionalization
Chiral Luttinger liquid

ABSTRACT

We study time dependent electronic transport along the chiral edge channels of the quantum Hall regime, focusing on the role of Coulomb interaction. In the low frequency regime, the a.c. conductance can be derived from a lumped element description of the circuit. At higher frequencies, the propagation equations of the Coulomb coupled edge channels need to be solved. As a consequence of the interchannel coupling, a charge pulse emitted in a given channel fractionalized in several pulses. In particular, Coulomb interaction between channels leads to the fractionalization of a charge pulse emitted in a given channel in several pulses. We finally study how the Coulomb interaction, and in particular the fractionalization process, affects the propagation of a single electron in the circuit. All the above-mentioned topics are illustrated by experimental realizations.

1. Introduction

The theoretical study of the dynamical properties of electronic transport in mesoscopic conductors has been pioneered by Markus Büttiker and his collaborators in the 1990s [1–4]. Following the description of the dc conductance of multichannel mesoscopic conductors as the coherent scattering of electronic waves [5], they studied the frequency dependent conductance $G(\omega)$ arising when the conductor terminals are driven by a time dependent voltage excitation. The latter case turns out to bring more complexity than the dc one, in particular as the role of Coulomb interaction is crucial. In the dc case, the current is expressed as a function of both the probability to be transmitted from one contact to the other and the difference between the electrochemical potentials of the contacts. In most of the cases, the effects of Coulomb interaction can be disregarded and remarkably, the conductance can be expressed as a function of the scattering amplitudes of non-interacting electronic waves. In the ac case, the time dependent current resulting from the variation of the electrochemical potential of the contacts gives rise to a time dependent accumulation of charges in the conductor which in turn leads to the variation of the electrostatic potential mediated by the long range Coulomb interaction. It is clear that this contribution to the ac current which directly stems from Coulomb interaction is crucial. Indeed, if one simply applied scattering theory as in the dc case, no current would be predicted to flow between contacts capacitively coupled, as scattering theory only predicts non-zero conductance between contacts which are physically connected by some transmission probability. The method introduced by Büttiker and coworkers in Refs. [1–4] follows two steps. In the first one, the ac current is calculated in a scattering formalism assuming a fixed value of the electrochemical potential of the contacts and of the electrical potential in the conductor. In the second one, the electrical potential is self-consistently calculated by relating the potential to the charges accumulated in the conductor using the capacitance matrix. Following these two steps, two time scales naturally appear. The first one, related to the non-interacting scattering description is the time of flight of non-interacting electron through the

* Corresponding author.
E-mail address: feve@lpa.ens.fr (G. Fève).

http://dx.doi.org/10.1016/j.physe.2015.10.006
1386-9477/

conductor of length l, $\tau_1 = l/v$. The second one is related to the Coulomb interaction through the conductor capacitance C and the typical impedance of a mesoscopic sample: $\tau_2 = hC/e^2$. Combining these two time scales by $1/\tau = v/l + e^2/hC$, one can define the important concept of electrochemical capacitance C_μ defined by $1/C_\mu = 1/C + hv/e^2l$, where the second term is the quantum capacitance of the conductor. The electrochemical capacitance is central to describe the effects of interactions in quantum conductors such as mesoscopic capacitors [1] but also the inductive like [4] behavior of quantum wires. Another major concept of time dependent transport is the charge relaxation resistance R_q [1] which together with the electrochemical capacitance defines the time it takes for charges to relax from the mesoscopic conductor to a macroscopic reservoir (contact). It differs from the dc resistance given by the Landauer formula. In particular, for a single mode quantum coherent conductor, $R_q = h/2e^2$ [1,6,7], independently of the probability for charges to be transmitted from the conductor to the reservoir. Remarkably, this universal behavior is robust to strong electron–electron interactions [8–10]. Mesoscopic capacitors and charge relaxation resistance have applications beyond the obvious understanding of the dynamics of charge transfer in mesoscopic conductors such as dephasing induced by charge fluctuations [11–13] or the efficiency of mesoscopic detectors [14,15].

The present paper will address more specifically time dependent electronic transport along the chiral edge channels of the quantum Hall regime. The motivation is twofold. Firstly, chiral edge channels provide an ideal system to test quantum laws of electricity beyond the dc limit. The ballistic and one dimensional nature of propagation, which can be implemented on long distances, realizes a simple set of interacting single mode quantum wires. However, one specificity of quantum Hall systems distinguishes them from usual wires: chiral propagation is enforced by the strong magnetic field. This specificity makes chiral edge channels particularly useful to study quantum coherence effects in time dependent situations. Indeed, the coherence of electron beams can be probed in electronic interferometers [16]. When time-dependent drives are applied, quantum coherent electronics can be pushed to the single electron scale where one studies the evolution of a single electron wavefunction in a quantum conductor. These electron quantum optics experiments [17] are the second motivation of this work. They have been pioneered by Markus Büttiker as well in many ways: mesoscopic capacitors are used as single electron emitters [18–20] which statistical properties can be accessed through the measurement of electronic noise [21–24] or the study of distribution of waiting times between successive electron emissions [25–27]. Next, the coherence properties of single electron states [28,29] can be probed in the electronic analog of the Hanbury–Brown and Twiss [30] or Hong–Ou–Mandel geometry [31] following a proposal by M. Büttiker and his collaborators [32] and paving the way for the coherent manipulations of a few charge quanta in quantum conductors based on multiparticle interference effects [33–35]. Remarkably, these experiments [36] have been so far well accounted for by the time dependent Floquet scattering theory [37,38] of the mesoscopic capacitor which builds on the generic scattering theory of time dependently driven mesoscopic conductors discussed above in the introduction.

While the study of single electron coherence is a strong motivation of the work presented in this paper, quantum coherence effects on time dependent transport will not be directly addressed. However, the purpose of the manuscript is to discuss the role of Coulomb interaction in charge propagation in quantum Hall systems and to connect it to the issue of single electron coherence. This question naturally arises as, on one hand, understanding and manipulating single electron coherence rely on a single-particle picture where interactions are disregarded. On the other hand, as mentioned above, Coulomb interaction plays a prominent role in time dependent charge propagation.

The paper will first review the lumped element description of Hall conductors at high frequency based on the calculation of the circuit emittance introduced in Ref. [39]. In particular the role of the electrochemical capacitance in the ac properties of Hall conductors will be extensively discussed. At higher frequency the lumped element description of the circuit breaks down and propagation effects need to be taken into account. The ac conductance then stems from the propagation of edge magnetoplasmons. The role of Coulomb interaction between edge channels will then be discussed as the coupling leads to the emergence of new propagation eigenmodes responsible for the fractionalization of the charge propagating in a given channel. Finally, fractionalization will be discussed at the single electron level, addressing the question of the death of the elementary quasiparticle caused by the Coulomb interaction. All the above-mentioned topics will be illustrated with various experimental realizations (with an emphasis put on our own). We would like to emphasize that the data presented are extracted from already published works. The purpose of this manuscript is to connect together various experimental approaches and discuss them in a unified theoretical framework inspired by the seminal works of Markus Büttiker and his collaborators.

2. Emittance of a Hall bar

We consider a generic quantum Hall circuit schematically represented in Fig. 1. Electronic transport occurs along the quantum Hall edge channels [40–42] located at the edges of the sample, the number of flowing channels at each edge being fixed by the number of occupied spin polarized Landau levels (the filling factor N). The metal-like edge channels are separated by dielectric regions [43]. They are electrically connected to ohmic contacts acting as electronic reservoirs and imposing the electrochemical potential V_α of the channels emerging from contact α. They are in capacitive influence with each other and with nearby metallic gates. In a time dependent situation, the electrochemical potential $V_\beta(t)$ of the reservoirs or gates is subject to a periodic modulation: $V_\alpha(t) = V_\alpha e^{-i\omega t}$. We are interested in the time dependent current response $I_\alpha(t)$ flowing from contact α, defining the multiterminal ac conductance:

$$I_\alpha = \sum_\beta G_{\alpha\beta}(\omega) V_\beta \tag{1}$$

For low enough drive frequency, $G_{\alpha\beta}(\omega)$ can be expanded at first order in ω, providing the first correction to the well known dc-conductance, see Eq. (2), and defining the emittance $E_{\alpha\beta}$ as done by Christen and Büttiker in Ref. [39].

$$G_{\alpha\beta}(\omega) = G^{(dc)}_{\alpha\beta} - i\omega E_{\alpha\beta} \tag{2}$$

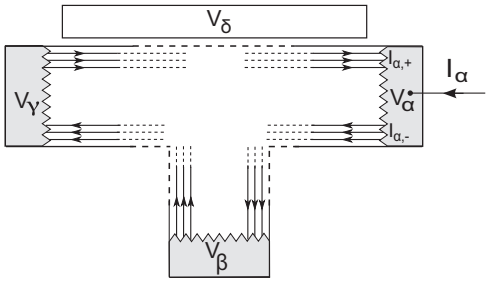

Fig. 1. Schematics of a generic Hall bar sample. Ohmic contacts and metallic gates are driven by time dependent electrochemical potentials V_α.

The following calculation of the emittance follows closely the one made in Ref. [39] with a few simplifications. We only consider here fully transmitted or fully reflected edge channels such that charges flowing in one channel emerge from a single contact and are injected to a single one. To distinguish edge channels from reservoirs, the edge channels are labeled by the roman indices k. To identify to which contacts the channels are connected, we use the notation $\Delta_{k\beta} = 1$ if channel k emerges from contact β (0 otherwise) and $\Delta_{\alpha k} = 1$ if edge channel k injects to contact α (0 otherwise). The edge channels are modeled as metallic wires with uniform electrical potential U_k along the sample edge. The electrochemical potential of channel k is imposed by the electrochemical potential V_β from which it emerges. The electrical potential U_k however is not imposed by the reservoir β. Its value depends on the charges accumulating in all the nearby conductors (edge channels and gates), and related by the capacitance matrix C describing the Coulomb interaction between the metallic conductors:

$$Q_k = \sum_j C_{kj} U_j. \tag{3}$$

The charge accumulating in edge channel k also equals the density of states of the channel times the energy difference between the electrochemical potential V_k and the band bottom U_k:

$$Q_k = D_k(V_k - U_k), \tag{4}$$

with $D_k = le^2/(hv_{D,k})$ represents the quantum capacitance of channel k which equals the electric charge times the density of states of a one dimensional wire of length l and drift velocity $v_{D,k}$. To simplify, we will assume all edges to have the same drift velocity v_D and same quantum capacitance such that $D_k = D_0$. Solving Eqs. (3) and (4) provides the dependence of all the electrical potentials U_k on the variations of the electrochemical potentials of the contacts V_β, defining the characteristic potentials $u_{k\beta}$:

$$U_k = \sum_\beta u_{k\beta} V_\beta. \tag{5}$$

The current I_α flowing from contact α is the difference between the current carried by the outgoing channels, $I_{\alpha,+}$ and the one carried by the incoming channels $I_{\alpha,-}$. The first one is related to the electrochemical potential V_α by the Landauer conductance while the second can be deduced from charge conservation on each channel k:

$$I_{\alpha,+} = \sum_k \Delta_{k\alpha} I_{k,+} = \frac{e^2}{h} \sum_k \Delta_{k\alpha} V_\alpha \tag{6}$$

$$I_{\alpha,-} = \sum_k \Delta_{\alpha k} I_{k,-} = \sum_k \Delta_{\alpha k} (I_{k,+} - \partial_t Q_k) \tag{7}$$

$$I_\alpha = \frac{e^2}{h} \sum_\beta \left(N_\beta \delta_{\alpha\beta} - \sum_k \Delta_{\alpha k} \Delta_{k\beta} \right) V_\beta - i\omega \sum_k \Delta_{\alpha,k} Q_k \tag{8}$$

where N_β is the total number of edge channels flowing from contact β and $\sum_k \Delta_{\alpha,k}\Delta_{k,\beta}$ represents the number of edge channels transmitted from contact β to contact α. The first term in factor of e^2/h is the usual dc conductance, the second one related to the charge accumulated in the edge channels is the emittance matrix. Using Eqs. (3)–(5), one immediately gets

$$E_{\alpha\beta} = \sum_k D_k \Delta_{\alpha k} (\Delta_{k\beta} - u_{k\beta}), \tag{9}$$

where the only quantities to be calculated are the characteristic potentials.

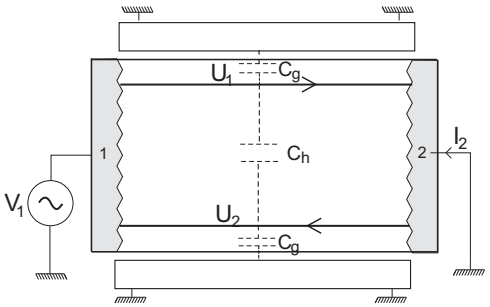

Fig. 2. Two terminal Hall bar. N channels are transmitted from contact 1 to contact 2. The electrical potential of the upper/lower edge channels is $U_{1/2}$. The edge channels are capacitively coupled to a grounded metallic gate with capacitance C_g. Counterpropagating channels are coupled by the capacitance C_h.

3. Examples, RL and RC circuits

We first consider the geometry depicted in Fig. 2 which consists of a Hall bar with two contacts at filling factor N such that N channels are connecting ohmic contact number 1 to Ohmic contact number 2. The edge channels on each side are interacting with a nearby gate with a capacitance C_g which represents interactions with the ground plane, and with each other through the mutual capacitance C_h (see Fig. 2). The capacitive coupling between co-propagating edge channels on the same side of the sample is supposed to be strong, such that they all share the same electrical potential $U_{1/2}$ for the upper/lower channels. The capacitance matrix relating the charges $Q_{1/2}$ to the potentials $U_{1/2}$ is given by

$$C = \begin{pmatrix} C_g + C_h & -C_h \\ -C_h & C_g + C_h \end{pmatrix} \tag{10}$$

We also assume equal density of states on each channels: $D_1 = D_2 = D = ND_0$.

Using Eqs. (3), (4) and (10), we obtain the characteristic potentials:

$$u_{11} = \frac{D(D + C_g + C_h)}{(D + C_g + 2C_h)(D + C_g)}, \quad u_{22} = u_{11} \tag{11}$$

$$u_{12} = \frac{DC_h}{(D + C_g + 2C_h)(D + C_g)}, \quad u_{21} = u_{12} \tag{12}$$

From which we get the emittance:

$$E_{21} = \frac{DC_g(D + C_g + 2C_h) + D^2 C_h}{(D + C_g + 2C_h)(D + C_g)} \tag{13}$$

$$G_{21} = -\frac{Ne^2}{h} - i\omega \frac{DC_g(D + C_g + 2C_h) + D^2 C_h}{(D + C_g + 2C_h)(D + C_g)} \tag{14}$$

E_{21} is positive which corresponds to an inductive behavior of the circuit. Given the sign conventions used in the paper, the serial association of a resistance R and an inductance L provides the following low frequency two terminal conductance: $G_{21} = -1/R - i\omega L/R^2$. The relation between the inductance of the Hall bar and the emittance is then given by $L = E_{21}/(Ne^2/h)^2$.

Two interesting limits can be discussed. The first one corresponds to the strong coupling between counterpropagating edges: $C_g \ll D, C_h$, $E_{21} \approx DC_h/(D + 2C_h) = C_{\mu h}$, where $C_{\mu h}$ is the electrochemical capacitance between the edges given by the serial association of the quantum capacitance D of the channels located on each side of the sample and the mutual capacitance C_h. The

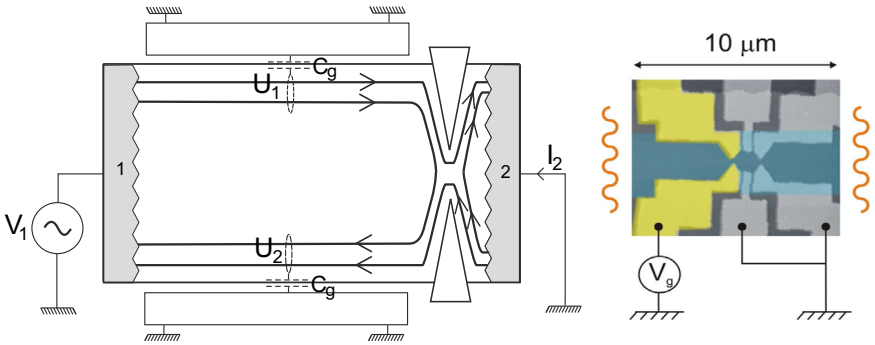

Fig. 3. Left panel: Schematics of the sample. A quantum point contact transmits T of the N edge channels from contact 1 to contact 2. The edge channels are capacitively coupled (with capacitance C_g to a grounded metallic gate. Counterpropagating edge channels are coupled by the capacitance C_h. Right panel: picture of the sample. The electron gas is colored in blue. The voltage V_g is applied on the gold top gate acting as a quantum point contact. Gray top gates are grounded and screen the Coulomb interaction. (For interpretation of the references to color in this figure caption, the reader is referred to the web version of this paper.)

inductance is then given by $L = C_{\mu h}/(Ne^2/h)^2$. If the coupling is very strong ($C_h \gg D$) corresponding to the limit of a non-chiral wire, $E_{21} \approx D/2$ giving $L = (h^2/e^4)D_0/2N$ which corresponds to the usual kinetic inductance of a quantum wire [44,45].

The relevant experimental situation is the limit of weak coupling between counterpropagating edges, $C_h \ll C_g$ in which case the emittance reduces to $E_{21} = DC_g/(D + C_g) = C_{\mu g}$, the electrochemical capacitance to the gate given by the serial association of the quantum capacitance D and the geometrical capacitance C_g. The inductance is then given by $L = C_{\mu g}/(Ne^2/h)^2$.

The differences between these two limits can be even more emphasized if one can vary the number T of channels transmitted from contact 1 to contact 2 using a quantum point contact (see Fig. 3), thereby changing the dc conductance (and resistance) of the wire, $G^{dc} = Te^2/h$, $R = h/Te^2$. For a classical circuit, one expects the value of the inductance not to vary when the resistance is modified, implying that E^{21} should vary like T^2. To compute the charges $Q_{1/2}$ accumulated on the upper and lower side of the Hall bar, we assume again that interchannel interaction is so strong that upper/lower channels have the same potential $U_{1/2}$. The only modification compared to the previous case is the change in the electrochemical potential of the lower channels as charges come both from contact 1 at V_1 (reflected channels) and from contact 2 at V_2 (transmitted channels).

$$Q_1 = ND_0(V_1 - U_1) = C_g U_1 + C_h(U_1 - U_2) \tag{15}$$

$$Q_2 = D_0\big(TV_2 + (N - T)V_1 - U_2\big) = C_g U_2 + C_h(U_2 - U_1) \tag{16}$$

$$u_{11} = \frac{ND_0\Big(\big(ND_0 + C_g + C_h\big(2 - \frac{T}{N}\big)\big)\Big)}{(ND_0 + C_g + 2C_h)(ND_0 + C_g)} \tag{17}$$

$$E_{21} = TD_0(1 - u_{11}) \tag{18}$$

$$E_{21} = \frac{TD_0C_g}{ND_0 + C_g} + \frac{T^2D_0^2C_h}{(ND_0 + C_g + 2C_h)(ND_0 + C_g)} \tag{19}$$

E_{12} is the sum of two terms, the second one varying like T^2 is the classical term, predicting a classical RL circuit which inductance L does not vary when the resistance R of the circuit is modified. The first term predicts an emittance linear in the dc conductance, meaning a constant phase of the complex conductance. This behavior cannot be understood as the serial addition of independent resistance and inductance. Looking at the dependence of the classical term, it emerges from the coupling between counterpropagating edges which tends to suppress the chiral nature of the Hall bar. For $C_h \gg C_g$, we have $E_{21} = (T^2/N^2)C_{\mu h}$ and we recover $L = C_{\mu h}/(Ne^2/h)^2$, the value of the inductance is independent of the number of transmitted channels. On the contrary, when chirality is preserved, $C_g \gg C_h$, $E_{21} = (T/N)C_{\mu g}$ and $L = (N/T)C_{\mu g}/(Ne^2/h)^2$. This expected difference shows up spectacularly in the phase of the ac conductance $\tan\phi = Im(G_{12})/Re(G_{12}) = \omega C_{\mu g}/(Ne^2/h)$ which becomes independent of the number of transmitted channels and only depends on the total number of channels (filling factor N).

The variation of the ac conductance of a Hall bar when the number of transmitted edge channels is modified has been checked experimentally in Ref. [46] on a 50 μm long and 6 μm wide Hall bar made in a GaAs/AlGaAs electron gas of nominal density $ns = 1.3 \times 10^{11}\,\mathrm{cm}^{-2}$ and mobility $\mu = 3 \times 10^6\,\mathrm{cm}^2\,\mathrm{V}^{-1}\,\mathrm{s}^{-1}$. The bar is interrupted in its middle by a pair of quantum point contacts (the right panel of Fig. 3). Only the first QPC is active with a negative voltage bias ($V_g \approx -1\,\mathrm{V}$) fully depleting the electron gas beneath it resulting in a small gate to 2DEG capacitance. The grounded gate of the second QPC widely overlaps the electron gas. This results in a large gate-2DEG capacitance $C_g \approx 30fF$ (for a gate length $l_g \approx 10\,\mu\mathrm{m}$) which efficiently screens the Coulomb interaction. Two values of the magnetic field have been investigated, $B = 0.224\,\mathrm{T}$ and $B = 0.385\,\mathrm{T}$ corresponding to filling factors $N=24$ and $N=14$ respectively. Fig. 4a represents the real and imaginary parts of the ac conductance (a drive frequency of 1.5 GHz) at $B = 0.385\,\mathrm{T}$, as a function of the gate voltage V_g (which controls the number of transmitted edge channels). Both the real and imaginary parts exhibit steps each time one additional channel goes through the QPC as V_g is varied. The step height is $2e^2/h$ for the real part of the conductance which equals twice the conductance quantum (spin degeneracy is not lifted). It is only coincidental that the steps in the imaginary part of the conductance are also close to $2e^2/h$. Fig. 4b shows a Nyquist representation ($Im(G)$ as a function of $Re(G)$) of the conductance. Remarkably, as a result of the chiral nature of the circuit, the phase stays constant when the number of transmitted channels is varied as can easily be seen on the Nyquist representation. As a comparison, the classical case of constant inductance ($L = 0.7\,\mu\mathrm{H}$) is represented in black dashed line, it clearly does not reproduce the data.

The constant phase observed in the Nyquist representation can be expressed as a transit time of charges through the Hall bar: $\tan\phi = \omega\tau_\rho$ defining a charge velocity renormalized by the screened Coulomb interaction: $v_\rho = l/\tau_\rho$ where l is the propagation length:

$$\tau_\rho = C_{\mu g}/(Ne^2/h) = l/(v_D + Ne^2/h\tilde{C}_g) \tag{20}$$

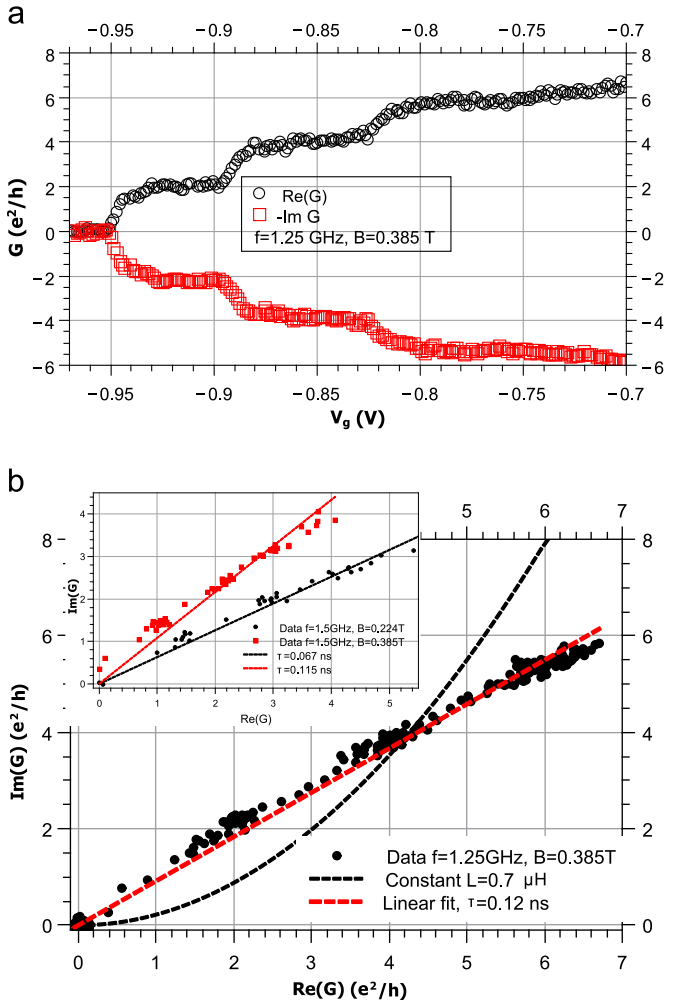

Fig. 4. (a) Real part $Re(G_{21})$ (black circles) and imaginary part (with minus sign) $-Im(G_{21})$ (red circles) as a function of the gate voltage V_g which controls the number of transmitted channels. (b) Nyquist representation of the conductance (imaginary part versus real part). Black dots represent the data ($f = 1.25$ GHz and $B = 0.385$ T). The red dashed line is a linear fit of the data. The black dashed line is the expected behavior for a classical circuit with constant inductance $L = 0.7$ μH. Data at $f = 1.5$ GHz and $B = 0.224$ T (black dots) and $B = 0.385$ T (red dots) are plotted in the inset with their linear adjustments (black and red lines). (For interpretation of the references to color in this figure caption, the reader is referred to the web version of this paper.)

$$v_\rho = v_D + Ne^2/(h\tilde{C}_g) \tag{21}$$

where $\tilde{C}_g$ is the geometrical capacitance per unit of gate length. From $\tau_\rho = 0.12$ ns extracted from a linear fit and the estimated gate length, $l_g \approx 10$ μm, we obtain a charge velocity $v_\rho \approx 10^5$ m s^{-1} in agreement with reported numbers in the literature [47,48] for gated samples. The inset of Fig. 4b shows measurements at different magnetic field and frequency. The extracted transit time is compatible with $\tau \propto B$, that is $v_\rho \propto 1/B$. As expected, the charge velocity is inversely proportional to the magnetic field.

A change from an inductive to a capacitive behavior should be expected when the QPC is fully pinched (see Fig. 5). In that case, the edge channels emerging from contact 1 are fully reflected back to contact 1 and charge transfer results from the capacitive coupling between counterpropagating edges reflected at the QPC with geometrical capacitance C_m. The charges Q_1 and Q_2 of edge channels emerging from contacts 1 and 2, their potentials, and the

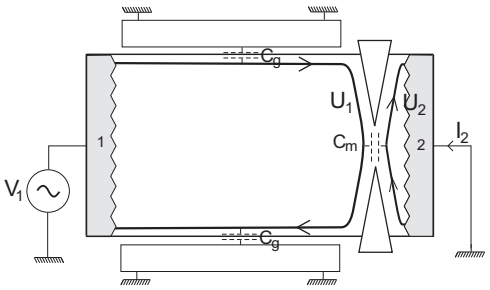

Fig. 5. Hall bar with fully pinched quantum point contact. Counterpropagating channels across the QPC are coupled by the capacitance C_m.

emittance E_{21} then read

$$Q_1 = ND_0(V_1 - U_1) = C_gU_1 + C_m(U_1 - U_2) \tag{22}$$

$$Q_2 = ND_0(V_2 - U_2) = C_gU_2 + C_m(U_2 - U_1) \tag{23}$$

$$u_{21} = \frac{ND_0C_m}{(ND_0 + C_g + 2C_m)(ND_0 + C_g)} \tag{24}$$

$$E_{21} = -ND_0u_{21} \tag{25}$$

$$E_{21} = -\frac{(ND_0)^2C_m}{(ND_0 + 2C_m)(ND_0 + C_g)} \tag{26}$$

The change of sign of the admittance in Eq. (26) compared to Eq. (13) reflects the change from an inductive to a capacitive behavior of the circuit. In the limit $ND_0 \gg C_g$, the coupling capacitance reduces to the electrochemical capacitance $C_{\mu m}$ between counterpropagating edges. This transition cannot be observed in Fig. 4 in our data, because $C_{\mu m}$ is small and hard to distinguish from the parasitic capacitive coupling between the contact pads. This transition has however be observed in ac measurements performed on a similar sample by Hashisaka and collaborators, Ref. [49]. Due to the geometry of their quantum point contact, counterpropagating channels run parallel to each others along a 50 μm length resulting in a large capacitive coupling when the QPC is closed ($C_{\mu m} \approx 3fF$). At the opening of the first channel, they observe the transition from a purely capacitive to an inductive regime. Interestingly, once the phase of the conductance has shifted from $-\pi/2$ (pure capacitance) to a positive value (inductance) at the opening of the first channel, the phase stays constant when an increasing number of channels are transmitted accordingly to our observation. The charge velocity v_ρ extracted from their measurements is higher than ours and lies in the 10^6 m s^{-1}. This difference is related to the absence in their sample of a metallic top gate covering the edge channels and efficiently screening the Coulomb interaction [48] (a lower value of $\tilde{C}_g$ leads to a larger charge velocity v_ρ). At frequencies higher than 1 GHz and large magnetic fields (filling factor $N \leq 4$) measurements in Ref. [49] are not compatible with the low frequency expansion at first order in ω of the conductance G, Eq. (2). In this high frequency regime, propagation effects must betaken into account, this will be the purpose of Section 5.

4. Interchannel interactions, $N=2$ case

The experiments described in the previous section do not allow

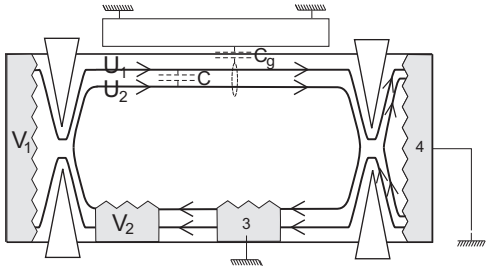

Fig. 6. Schematics of the two QPC sample allowing to selectively address the electrochemical potential of each copropagating channels 1 and 2. Electrochemical potential of channel 1/2 is $V_{1/2}$. Two output configurations are studied: either channels 1 and 2 are both reflected to contact 3 (configuration 1) or only channel 2 is reflected towards 3 (configuration 2).

to probe interactions between co-propagating channels. Indeed, co-propagating edge channels are connected to the same contact, they share the same electrochemical potential and are excited in a symmetric fashion. In this situation, one only probes the propagation velocity of the total charge carried by all the co-propagating channels, which is more sensitive to the coupling to the screening gate than to the coupling between edges. However, the study and characterization of interchannel interactions are central to understand energy relaxation [50,51] and the loss of electronic coherence in quantum Hall edge channels [52,53]. It has indeed been shown that Coulomb interactions were directly responsible for these phenomena [54–57].

The simplest situation to study inter-channel interaction is the $N=2$ case, where propagation occurs along two spin polarized channels. In order to impose different electrochemical potentials to the two channels, we consider the sample depicted in Fig. 6. A quantum point contact is set to selectively transmit [42] the outer edge and fully reflect the inner one, such that edge channels 1 and 2 emerge from two different ohmic contacts 1 and 2. A second quantum point contact placed after a propagation length l can be used either to reflect both channels towards contact 3 (case 1) or to reflect only the inner channel towards 3 (case 2). We first consider the case where only V_1 is time dependently driven such that current is only injected in the outer edge channel 1 at the input of the inter-edge interaction region. As in the previous section, both edge channels are assumed to have the same quantum capacitance D_0, they are coupled to the ground plane through the capacitance C_g and to each other through the inter-channel capacitance C. We compute the emittance in the two above-mentioned cases. In the first one, both edge channels are connected to the output contact 3, and $E_{31}^{(1)} = D_0(1 - u_{1,1} - u_{21}) = D_0 C_g/(D_0 + C_g)$. The result is very similar to the emittance of the Hall bar obtained in the previous section. The phase of the complex conductance $G_{31}^{(1)} = -e^2/h(1 + i\omega l/v_\rho)$ encodes the transit time of charges in the interaction region with a charge velocity renormalized by the screened Coulomb interaction that can be expressed as a function of the electrochemical capacitance to the gate:

$$v_\rho = v_D + \frac{e^2}{h\tilde{C}_g} = \frac{e^2}{h\tilde{C}_{\mu g}} \tag{27}$$

In the second case, the output quantum point contact is set to reflect only the inner channel towards contact 3. This setup directly measures the current transferred from the outer to the inner channel as a result of the inter-channel interaction. Considering a weak coupling to the gate ($C_g \ll C, D_0$), we obtain

$$E_{31}^{(2)} = -D_0 u_{21} = -\frac{D_0 C}{2C + D_0} \tag{28}$$

$$G_{31}^{(2)} = i\omega \frac{D_0 C}{2C + D_0} = i\omega C_\mu. \tag{29}$$

The change of sign of the emittance from configuration (1) to configuration (2) reflects the change from an inductive to a capacitive behavior. The capacitance equals the electrochemical capacitance C_μ between the inner and outer channels given by the serial association of the quantum capacitance D_0 of each channel and the geometrical capacitance C. As expected from this purely capacitive coupling, the output current is purely imaginary such that no timescale or transit time can be associated to the conductance phase. However, it is possible to define a characteristic time τ_n from $E_{31}^{(2)}$ by dimensional arguments: $\tau_n = 2E_{31}^{(2)}/(e^2/h)$. Following the same line of thought, a velocity $v_n = l/\tau_n$ can be defined

$$\tau_n = \frac{l}{v_D + e^2/(2h\tilde{C})} \tag{30}$$

$$v_n = v_D + \frac{e^2}{2h\tilde{C}} = \frac{e^2}{2h\tilde{C}_\mu} \tag{31}$$

where $\tilde{C} = C/l$ and $\tilde{C}_\mu = C_\mu/l$ are the geometrical and electrochemical capacitances per unit length. To provide an interpretation of this transit time and of this velocity, one can consider the case where both ohmic contacts 1 and 2 are driven by voltage excitations at the same pulsation ω but with opposite amplitudes $V_2 = -V_1$. This generates opposite or antisymmetric charge distributions along edge channels 1 and 2. As such, the total current collected in configuration (1) when both edge channels are deflected towards ohmic contact 3 vanishes: $I^{(1)} = (G_{31}^{(1)} - G_{32}^{(1)})V_1 = 0$ (where $G_{31}^{(1)} = G_{32}^{(1)}$ directly results from the symmetry between edge channels 1 and 2 assumed in the previous discussions). This antisymmetric charge distribution is thus a neutral excitation which does not carry a total charge when summed on both channels. To get the propagation velocity of this neutral excitation through a standard current measurement, one must use configuration (2) so as to measure only the current carried by the inner edge channel at the output of the interaction region, $I^{(2)} = (G_{31}^{(2)} - G_{32}^{(2)})V_1$. $G_{31}^{(2)} = -i\omega E_{31}^{(2)}$ as calculated above. From symmetry between channels and current conservation arguments, we get, $G_{32}^{(2)} = G_{41}^{(2)} = G_{31}^{(1)} - G_{31}^{(2)}$, providing:

$$I^{(2)} = \left(2G_{31}^{(2)} - G_{31}^{(1)}\right)V_1 = \frac{e^2}{h}\left(1 + i\omega\frac{D_0 C}{C + D_0/2}\right)V_1 \tag{32}$$

$$\tan\phi = \omega\tau_n = \omega l/v_n \tag{33}$$

The velocity v_n introduced above from dimensional arguments and related to the interchannel coupling C thus probes the propagation velocity of a neutral antisymmetric charge distribution between both channels. The velocity v_ρ related to the coupling to the screening gate C_g probes the velocity of the total charge (symmetric distribution between the channels).

To probe interchannel interactions through high frequency conductance measurements, we used in Ref. [58] a geometry different than the one proposed in Fig. 6. The sample is presented in Fig. 7. To inject current in the outer channel, we use a mesoscopic capacitor [1,7]. The outer edge channel (1) is selectively transmitted in a cavity which is capacitively coupled to a metallic top gate on which we apply the RF excitation. The ac current at the output of the $l = 3.2 \pm 0.4\,\mu$m interaction region is measured on ohmic contact 3. Configurations (1) and (2) are selected by changing the gate voltage V_{qpc} applied on the output quantum point contact. To avoid gain and phase calibrations, we measure the ratio

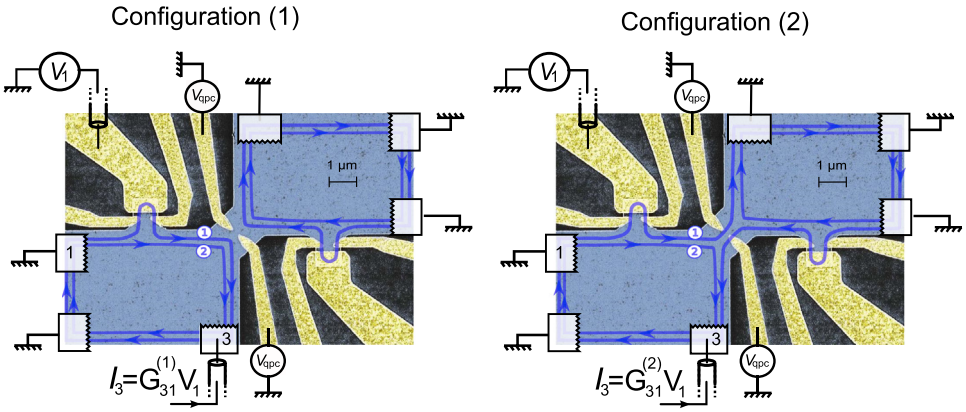

Fig. 7. Modified scanning electronic microscope picture of the sample. The electron gas is in blue, metallic gates in gold, and edge channels 1 and 2 are represented by blue lines. Selective current injection on the outer edge channel (1) is performed by capacitively coupling edge channel 1 only to a metallic top gate on which time dependent voltage V_1 is applied. The current at the output of the $l \approx 3\,\mu m$ interaction region is measured in configuration 1 (left panel) and in configuration 2 (right panel). (For interpretation of the references to color in this figure caption, the reader is referred to the web version of this paper.)

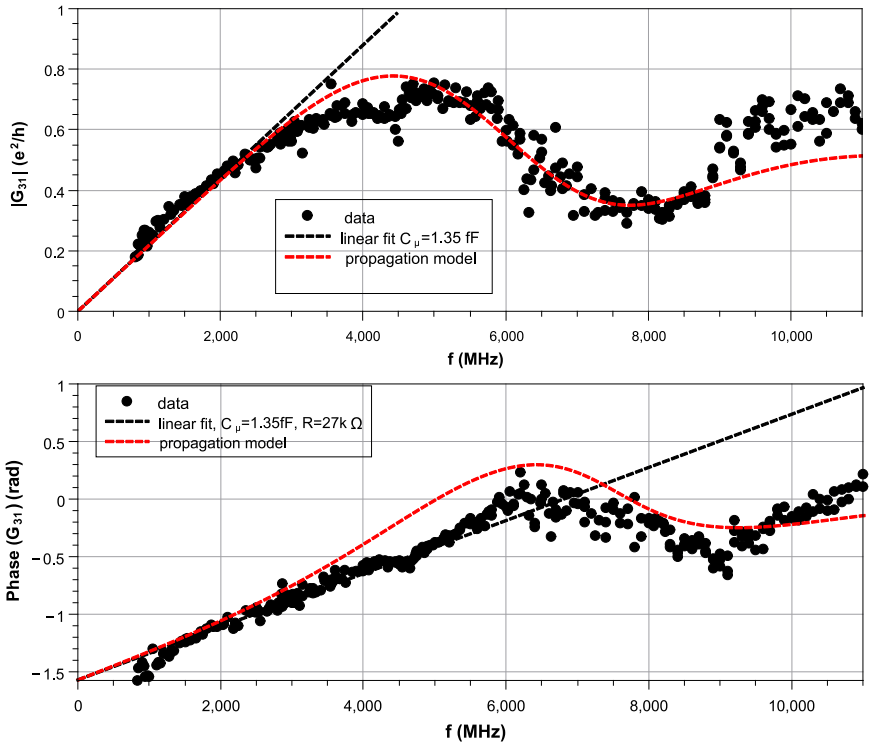

Fig. 8. Modulus (upper panel) and phase (lower panel) of the conductance $G_{31}^{(2)}$ normalized $G_{31}^{(1)}$ as a function of frequency. The data are represented by black dots, low frequency linear adjustments by black dashed lines. The red dashed lines represents the predictions of the propagation model Eq. (52) with parameters $C_\mu = 1.35\ fF$ ($v_n = 4.6 \times 10^5\ m\ s^{-1}$), imposed by the low frequency behavior, $v_D = 2.25 \times 10^4\ m\ s^{-1}$, imposed by the high frequency behavior, and $\tau_r = 4.1$ ps. (For interpretation of the references to color in this figure caption, the reader is referred to the web version of this paper.)

of the conductance in the two configurations, $\mathcal{R} = G_{31}^{(2)}(\omega)/G_{31}^{(1)}(\omega)$ as a function of the drive frequency from 1 GHz to 11 GHz. Assuming $C_g \ll C$, we have $v_\rho \gg v_n$ and $G_{31}^{(1)}(\omega) \approx e^2/h$ such that $\mathcal{R}$ measures $G_{31}^{(2)}(\omega)$ in units of e^2/h. Measurements of the modulus and phase of $G_{31}^{(2)}(\omega)$ as a function of frequency are presented in Fig. 8. At low frequency ($f \leq 2.5$ GHz), both the modulus and phase of the conductance evolve linearly with frequency (see the linear fits represented by the black dashed lines). The zero frequency intercept of the modulus is zero, while the phase goes to $\pi/2$. This low frequency dependence agrees with the capacitive coupling described by Eq. (29) with an electrochemical coupling capacitance $C_\mu = 1.35fF \pm 0.15fF$, that is a neutral mode velocity of $v_n = 4.6 \pm 0.5 \times 10^5\ m\ s^{-1}$. The linear dependence of the phase with frequency provides the ω^2 term in the power expansion of $G_{31}^{(2)}(\omega)$:

$$G_{31}^{(2)}(\omega) = i\omega C_\mu (1 + i\omega R C_\mu), \tag{34}$$

corresponding to the serial addition of a capacitance and a resistance. From the slope of the linear dependence of the phase with frequency, we deduce $R = 27 \pm 3.5k\Omega \approx h/e^2$. This is in agreement with Refs. [1] and [7] investigating the charge relaxation resistance in an ac driven RC circuit. As discussed in the introduction, it equals $h/(2e^2)$ for a single spin polarized channel. Here charge transfer occurs from a single spin polarized channel to another single spin polarized channel, charge relaxation resistance thus equals twice $h/2e^2$.

At frequencies higher than 3 GHz, the lumped element circuit description limited in second order in ω cannot account for the frequency dependence of the ac conductance which exhibits an oscillating behavior. For such high frequencies, the wavelength of

the propagating modes becomes comparable with the circuit size (few microns) and the uniform potential assumption valid at low frequency does not hold anymore. One needs to take into account propagation effects along the edge channels.

5. Propagation and edge-magnetoplasmons

At high frequencies, one cannot neglect the space dependence of the currents $I_k(x, t)$, charge densities $\rho_k(x, t)$ and electrical potential $U_k(x, t)$ at position x of edge channel k. Current propagation is then described in terms of edge magnetoplasmon modes which circulate at the edges of the sample [59–61]. The charge density $\rho_k(x, t)$ is related to $I_k(x, t)$ through the usual current conservation equation: $\partial_x I_k + \partial_t \rho_k = 0$. The propagation equation for the current [62] is obtained by considering the sum of two contributions. The first one comes from the excess charge ρ_k moving at the drift velocity $v_{D,k}$, the second one comes from the Hall current $(e^2/h)U_k$ caused by the variation of the channel potential. Focusing on a harmonic variation of the current, potential and charge at pulsation ω, we get

$$I_k(x, t) = \rho_k(x, t)v_{D,k} + \frac{e^2}{h}U_k(x, t) \tag{35}$$

$$(-i\omega + v_{D,k}\partial_x)I_k(x) = -\frac{i\omega e^2}{h}U_k(x) \tag{36}$$

The potential $U_k(x)$ is related to the charge densities of all other edge channels and conductors by the long range Coulomb interaction:

$$U_k(x) = \sum_j \int dy U_{kj}(x, y)\rho_j(y) \tag{37}$$

We start first with the simple limit of shirt range Coulomb interaction: $U_{kj}(x, y) = U_{kj}\delta(x - y)$. Note that this crude assumption will always be valid at low enough frequency, when the wavelength of the propagation modes are larger than the interaction range. In this limit, the interaction parameters U_{kj} identify to the inverse capacitance matrix elements per unit length: $\tilde{C}_{ij}^{-1}$:

$$U_k(x) = \sum_j \tilde{C}_{ij}^{-1}\rho_j(x), \tag{38}$$

and the current propagation equation can be rewritten introducing the velocity matrix v with $v_{ij} = v_{D,i}\delta_{ij} + (e^2/h)\tilde{C}_{ij}^{-1}$:

$$(-i\omega\mathbb{I} + v\partial_x)I(x) = 0 \tag{39}$$

where $\mathbb{I}$ is the identity matrix and $I(x)$ is the vector of the currents propagating along the edge channels.

Eq. (39) lends itself to a description in terms of voltage and current propagation in a unidirectional transmission line [63]. The electrochemical potential of edge channel k, $V_k(x, t)$, is the sum of the electrical potential $U_k(x, t)$ and the chemical potential $\rho_k(x, t)/\tilde{D}_0$ (where $\tilde{D}_0$ is the quantum capacitance per unit length). As such, $V_k(x, t)$ also depends on the position x along the edge channel and is very simply related to the current $I_k(x, t)$:

$$V_k(x, t) = U_k(x, t) + \frac{h}{e^2}\rho_k(x, t)v_D = \frac{h}{e^2}I_k(x, t) \tag{40}$$

Eqs. (39) and (40) describe current propagation in terms of coupled unidirectional transmission lines of characteristic impedances $R_K = h/e^2$. Let us discuss first the simple case $N=1$ where a single line is involved with charge velocity $v_\rho = (e^2/h)1/\tilde{C}_{\mu g}$. Then current propagation can be described as a distributed LC line (se Fig. 9a) with a capacitance to the ground $\tilde{C}_{\mu g}$ and an inductance $\tilde{L} = (h^2/e^4)\tilde{C}_{\mu g}$ per unit length. When several lines are coupled, the

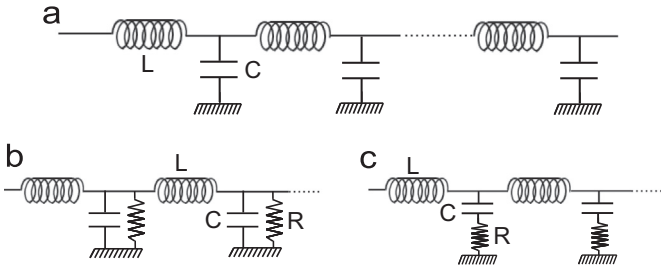

Fig. 9. (a) Transmission line description of propagation, $C = C_{\mu g}$, $L = (h^2/e^4)C_{\mu g}$. (b) Dissipative transmission line with resistance R to the ground. (c) Dissipative transmission line with resistance R in series with the capacitance $C_{\mu g}$.

solutions of Eq. (39) are found by diagonalizing the matrix v. Labeling I_λ an eigenmode of the velocity matrix and v_λ the eigenvalue, we obtain $I_\lambda(x, t) = I_\lambda e^{i\omega(x/v_\lambda - t)}$.

In the specific case where two copropagating channels are considered, the velocity matrix and its eigenvalues read

$$v = \begin{pmatrix} v_D + \frac{e^2}{h}\frac{\tilde{C}_g + \tilde{C}}{\tilde{C}_g(\tilde{C}_g + 2\tilde{C})} & \frac{e^2}{h}\frac{\tilde{C}}{\tilde{C}_g(\tilde{C}_g + 2\tilde{C})} \\ \frac{e^2}{h}\frac{\tilde{C}}{\tilde{C}_g(\tilde{C}_g + 2\tilde{C})} & v_D + \frac{e^2}{h}\frac{\tilde{C}_g + \tilde{C}}{\tilde{C}_g(\tilde{C}_g + 2\tilde{C})} \end{pmatrix} \tag{41}$$

$$v_\rho = v_D + \frac{e^2}{h}\frac{1}{\tilde{C}_g} = \frac{e^2}{h\tilde{C}_{\mu g}}, \quad I_\rho = I_1 + I_2 \tag{42}$$

$$v_n = v_D + \frac{e^2}{h}\frac{1}{\tilde{C}_g + 2\tilde{C}} = \frac{e^2}{2h\tilde{C}_\mu}\ (\tilde{C}_g \ll \tilde{C}), \quad I_n = I_1 - I_2 \tag{43}$$

Note that we restricted ourselves to the case of identical channels ($\tilde{C}_{g1} = \tilde{C}_{g2} = \tilde{C}_g$, $v_{D1} = v_{D2} = v_D$) which imposes the nature of the eigenmodes: the symmetric charge mode and the antisymmetric neutral mode already introduced in the previous sections. Different eigenmodes could be obtained considering that channels 1 and 2 are different. However, if the interchannel interaction is stronger than the asymmetry between channels : $v_{12} \gg (v_{11} - v_{22})/2$ (strong interaction regime), one recovers the charge and neutral eigenmodes.

The propagation model now allows us to calculate the currents at all orders in the drive pulsation ω. Decomposing the edge currents I_1 and I_2 on the eigenmode basis, we can express $I_1(x = l)$ and $I_2(x = l)$ as a function of their input values $I_1(x = 0)$ and $I_2(x = 0)$ using the 2×2 scattering matrix $S(\omega, l)$ [64,55]:

$$I(\omega, l) = S(\omega, l)I(\omega, 0) \tag{44}$$

$$\begin{pmatrix} I_1(l) \\ I_2(l) \end{pmatrix} = \begin{pmatrix} \frac{e^{i\omega l/v_\rho} + e^{i\omega l/v_n}}{2} & \frac{e^{i\omega l/v_\rho} - e^{i\omega l/v_n}}{2} \\ \frac{e^{i\omega l/v_\rho} - e^{i\omega l/v_n}}{2} & \frac{e^{i\omega l/v_\rho} + e^{i\omega l/v_n}}{2} \end{pmatrix} \begin{pmatrix} I_1(0) \\ I_2(0) \end{pmatrix} \tag{45}$$

The conductance is then calculated first by relating $I_1(0)$ and $I_2(0)$ to the electrochemical potentials of the contacts to which they are connected: $I_1(0) = e^2/hV_1$, $I_2(0) = 0$. Secondly by summing the output currents measured in contact 3: $I_1(l) + I_2(l)$ in configuration (1), $I_2(l)$ only in configuration (2). We obtain the following ac conductances in configurations (1) and (2) as a function of the scattering coefficients $S(\omega, l)$:

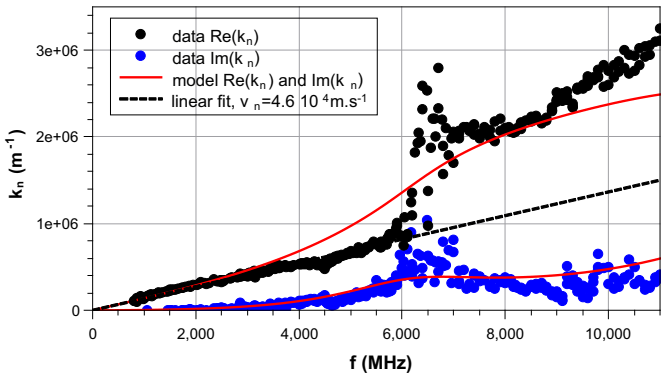

Fig. 10. Real (black dots) and imaginary (red dots) parts of the wavevector k_n as a function of frequency. The black dashed line represents the constant velocity prediction (short range model). The red lines represent the full propagation model including attenuation and long range interaction with parameters $C_\mu = 1.35$ fF ($v_n = 4.6 \times 10^4$ m s^{-1}), imposed by the low frequency behavior, $v_D = 2.25 \times 10^4$ m s^{-1}, imposed by the high frequency behavior, and $\tau_r = 4.1$ ps. (For interpretation of the references to color in this figure caption, the reader is referred to the web version of this paper.)

$$G_{31}^{(1)}(\omega) = \frac{e^2}{h}(S_{11} + S_{21}) = \frac{e^2}{h}e^{i\omega l/v_\rho} \tag{46}$$

$$G_{31}^{(2)}(\omega) = \frac{e^2}{h}S_{21} = \frac{e^2}{h}\frac{e^{i\omega l/v_\rho} - e^{i\omega l/v_n}}{2} \approx \frac{e^2}{h}\frac{1 - e^{i\omega l/v_n}}{2} \tag{47}$$

Eq. (47) describes an oscillatory behavior as a function of either interaction length l or pulsation ω. The current injected in the outer channel oscillates from the outer to the inner channel and back to the outer channel again. Such a behavior agrees qualitatively with the one observed in Fig. 8, where the modulus of $G_{31}^2(\omega)$ increases up to ≈ 0.75 then decreases back down to ≈ 0.35 and rises up again to ≈ 0.7. Contrary to Eq. (47), $G_{31}^2(\omega)$ does not go up to 1 then back down to zero, this attenuated oscillation signals the presence of dissipation in the propagation. To capture the dissipation in the propagation process, we can rewrite the phase factor $\omega l/v_n$ as $k_n l$ where k_n is the wavevector of the neutral mode. k_n extracted from the measurements of G_{31}^2 by inverting Eq. (47) is plotted in Fig. 10. As discussed above, dissipation is present and shows up as an imaginary part of k_n which vanishes at low frequency. The real part of k_n evolves linearly with frequency up to $f \approx 6$ GHz, which is consistent with a frequency independent velocity $v_n = 4.6 \times 10^4$ m s^{-1}. At higher frequencies, $Re(k_n)$ deviates from a linear variation to reach again a linear evolution but with a different slope: $v_n(\omega \to \infty) = 2.25 \times 10^4$ m s^{-1}. This ω dependence of the velocity is not predicted by the short range interaction model presented above. It results from the finite range of interaction. In the limit of high frequencies, when the wavelength of the propagating modes becomes smaller than the interaction range, the role of interaction in the propagation velocity is suppressed and one recovers the non-interacting drift velocity v_D. We can thus attribute the high limit of the velocity to the non-interacting value, $v_D = 2.25 \times 10^4$ m s^{-1}. In order to add an interaction range in the model, we assume that the interaction between $\rho_i(x)$ and $\rho_j(y)$ does not depend on the distance $x - y$ (for $0 \le x, y \le l$). This crude assumption imposes an interaction range which equals the length of the interaction region l. $U_{k,j}(x, y)$ then becomes independent of x and y, $U_{k,j}(x, y) = U_{kj}$ where U_{kj} identify to the inverse capacitance matrix elements C_{kj}^{-1}. $U_k(x)$ becomes independent of x and Eq. (37) can be rewritten as

$$U_k = \sum_j U_{kj} \int dy \rho_j(y) = \sum_j C_{kj}^{-1} Q_j \tag{48}$$

Dissipation can also be taken into account by adding a dissipative term in Eq. (36). Several possibilities can be considered which can be illustrated by the unidirectional transmission line model. Let us consider first the simple case of a single uncoupled line. Dissipation can first be added by considering that some current leaks to the ground for example through the bulk of the electron gas (see Fig. 9b). A second possibility is to consider that the line is capacitively coupled to a dissipative conductor before reaching the ground (see Fig. 9c). Computing the propagation equation and the dispersion relation $k(\omega)$ in these two cases provide very different results:

$$k(\omega)^{(1)} = \sqrt{\tilde{L}\tilde{C}_{\mu g}}\left(\omega + \frac{i}{\tau_r}\right), \quad \tau_r = R\tilde{C}_{\mu g}, \quad \omega\tau_r \gg 1 \tag{49}$$

$$k(\omega)^{(2)} = \sqrt{\tilde{L}\tilde{C}_{\mu g}}\ \omega(1 + i\omega\tau_r), \quad \tau_r = \frac{R\tilde{C}_{\mu g}}{2}, \quad \omega\tau_r \ll 1 \tag{50}$$

$k(\omega)^{(1)}$ describes an attenuation which does not depend on frequency such that dc current also leaks to the ground. The frequency independent damping does not properly account for our observation of $Im(k_n)$ in Fig. 10. On the contrary, $k(\omega)^{(2)}$ describes a damping increasing with frequency which fits more our observation. We thus choose to add the $\gamma(\omega) = \omega^2\tau_r$ term in the propagation equation (36):

$$(-i\omega + \omega^2\tau_r + v_D\partial_x)I_k(x) = -\frac{i\omega e^2}{h}\sum_j C_{kj}^{-1}Q_j \tag{51}$$

Solving Eq. (51), we obtain the current $I_2(l)$ as a function of the input current $I_1(0)$:

$$I_2(l) = \frac{1 - e^{i\omega\tau_D}e^{-\omega^2\tau_r\tau_D}}{2 + \frac{i}{(\omega + i\omega^2\tau_r)\tau_C}(1 - e^{i\omega\tau_D}e^{-\omega^2\tau_r\tau_D})} \times I_1(0) \tag{52}$$

with $\tau_D = l/v_D$ and $\tau_C = R_K C$. Eq. (52) obeys the same low frequency behavior as the discrete element model, Eq. (29) and the propagation model with short range interaction, Eq. (47), with the same expression for the electrochemical capacitance C_μ. At second order in ω, the charge relaxation resistance is slightly modified by dissipation effects and increases by $\tau_r/2C_\mu$ compared to the dissipationless value h/e^2 with $\tau_r e^2/2C_\mu h \ll 1$ if dissipation is small. The effect of the interaction range only appears at high frequency when the neutral mode wavelength becomes comparable with l. Predictions of Eq. (52) are plotted (red lines) in Figs. 8 and 10. Parameters are $C_\mu = 1.35fF$ (imposed by the low frequency behavior) and $\tau_r = 4.1$ ps (adjustable parameter), $v_D = 2.25 \times 10^4$ m s^{-1} (imposed by the high frequency behavior of Fig. 10). The model captures the period of the oscillations of the modulus as well as the attenuation of the amplitude of these oscillations. In Fig. 10, it reproduces well the attenuation and captures the change in velocity as a function of the frequency although the change of velocity is much sharper in the experiment.

Another complementary simple geometry investigated in Refs. [63] and [65] to study Coulomb interaction effects between two edge channels is the $N=1$ case when two counterpropagating channels are brought close enough (see Fig. 11) such that their mutual interaction cannot be neglected. A 1 μm wide and ≈50 μm long gate, on which a negative voltage is applied so as to deplete the electron gas underneath, is used to define an interaction region between the two single counterpropagating edge channels located on each side of the metallic gate. Compared to the co-propagating case, the opposite velocities of the two initially non-

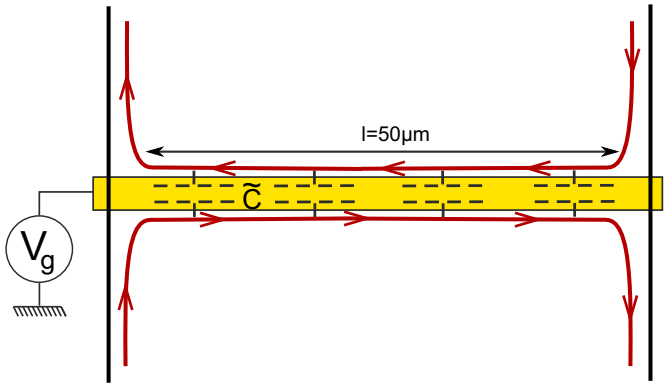

Fig. 11. Interaction between counterpropagating channels as implemented in Ref. [65]. At filling factor $\nu=1$, a single edge channel (represented in red) propagates at the edges of the sample. A metallic gate (yellow on the sketch) is biased with a negative voltage V_g in order to deplete the electron gas underneath. Two counterpropagating edge channels separated by the gate width of approximately 1 μm interact through the Coulomb interaction on the gate length $l \approx 50$ μm. Assuming short range interaction, the interchannel interaction can be modeled by the capacitance per unit length $\tilde{C}$. (For interpretation of the references to color in this figure caption, the reader is referred to the web version of this paper.)

interacting edge magnetoplasmons give rise to different eigenmodes when interchannel Coulomb interaction is turned on. Compared to Eq. (41), the sign of the velocities is changed for edge channel 2 in the velocity matrix:

$$v = \begin{pmatrix} v_D + \frac{e^2}{h}\frac{\tilde{C}_g+\tilde{C}}{\tilde{C}_g(\tilde{C}_g+2\tilde{C})} & \frac{e^2}{h}\frac{\tilde{C}}{\tilde{C}_g(\tilde{C}_g+2\tilde{C})} \\ -\frac{e^2}{h}\frac{\tilde{C}}{\tilde{C}_g(\tilde{C}_g+2\tilde{C})} & -v_D - \frac{e^2}{h}\frac{\tilde{C}_g+\tilde{C}}{\tilde{C}_g(\tilde{C}_g+2\tilde{C})} \end{pmatrix} \tag{53}$$

The eigenvalues and eigenmodes of v are given by

$$v_{+/-} = \pm\sqrt{\left(v_D + \frac{e^2}{h\tilde{C}_g}\right)\left(v_D + \frac{e^2}{h(\tilde{C}_g+2\tilde{C})}\right)} \tag{54}$$

$$v_{+/-} = \pm\sqrt{v_\rho v_n} \tag{55}$$

$$I_+ = I_1 - rI_2 \quad I_- = I_2 - rI_1 \tag{56}$$

$$r = \frac{v_D + \frac{e^2}{h}\frac{\tilde{C}_g+\tilde{C}}{(\tilde{C}_g+2\tilde{C})\tilde{C}_g} - \sqrt{\left(v_D + \frac{e^2}{h\tilde{C}_g}\right)\left(v_D + \frac{e^2}{h(\tilde{C}_g+2\tilde{C})}\right)}}{\frac{e^2}{h}\frac{\tilde{C}}{(\tilde{C}_g+2\tilde{C})\tilde{C}_g}} \tag{57}$$

The two eigenmodes have opposite velocities which is reminiscent of the initial non-interacting case. Due to the coupling between the edge channels, the charge of the eigenmodes is distributed on both channels. In the example of the eigenmode I_+, the current I_1 propagating on channel 1 in the forward direction drags the charge $-rI_1$ on edge channel number 2 in the interaction region. In the strong interchannel interaction limit, $\tilde{C}$, $D_0 \gg \tilde{C}_g$, $r \to 1$ and $v_\pm \to \pm e^2/h\sqrt{2\tilde{C}_{\mu g}\tilde{C}_\mu}$, the eigenmodes in the interaction region correspond to antisymmetric charge distributions propagating in the forward or backward direction. In the small interchannel interaction limit which corresponds to the relevant experimental situation of Ref. [65], $\tilde{C}_g$, $D_0 \gg \tilde{C}$, $r \to \tilde{C}/2\tilde{C}_g \ll 1$ and $v_\pm \to \pm e^2/h\tilde{C}_{\mu g}$. Only a small portion $-r$ of the input charge carried in channel 1 is dragged on channel 2 in the interaction region.

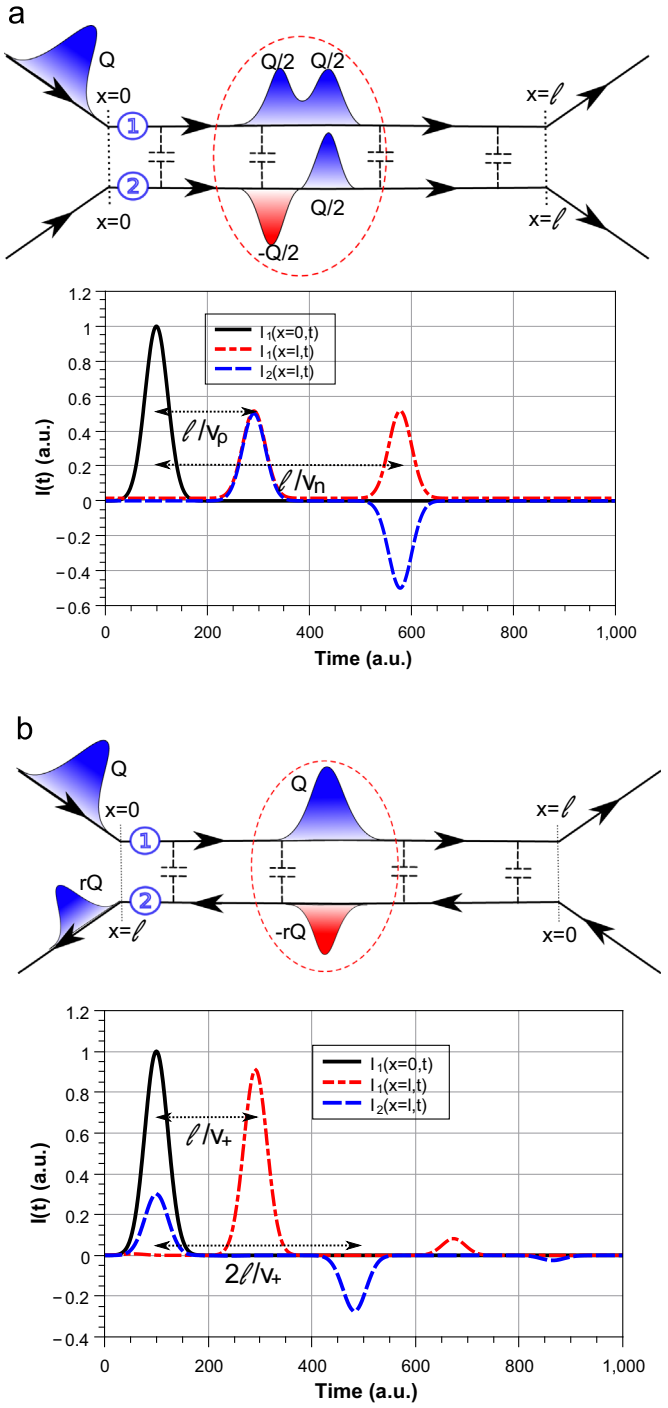

Fig. 12. (a) Upper panel: sketch of charge fractionalization in situation 1. The input charge pulse in channel 1 splits in a charge and neutral eigenmode. Lower panel: simulations of the input $I_1(x=0,t)$ and output $I_1(x=l,t)$, $I_2(x=l,t)$ with $v_\rho = 2.5v_n$. (b) Upper panel: sketch of charge fractionalization in situation 2. The input charge pulse in channel 1 drags the charge $-rQ$ in channel 2 in the interaction region. Due to charge conservation, the pulse rQ is generated at $t=0$ and $x=l$ in channel 2. Lower panel: simulations of the input $I_1(x=0,t)$ and output $I_1(x=l,t)$, $I_2(x=l,t)$ with $r=0.3$. The successive pulses result from successive reflections at the edges of the interaction region and are separated by the delay $2l/|v_\pm|$. (For interpretation of the references to color in this figure caption, the reader is referred to the web version of this paper.)

6. Interchannel coupling and charge fractionalization

Charge fractionalization in the integer quantum Hall regime [65–69] occurs when a current pulse carrying charge Q is incoming at the input of the interchannel interaction region. There, as

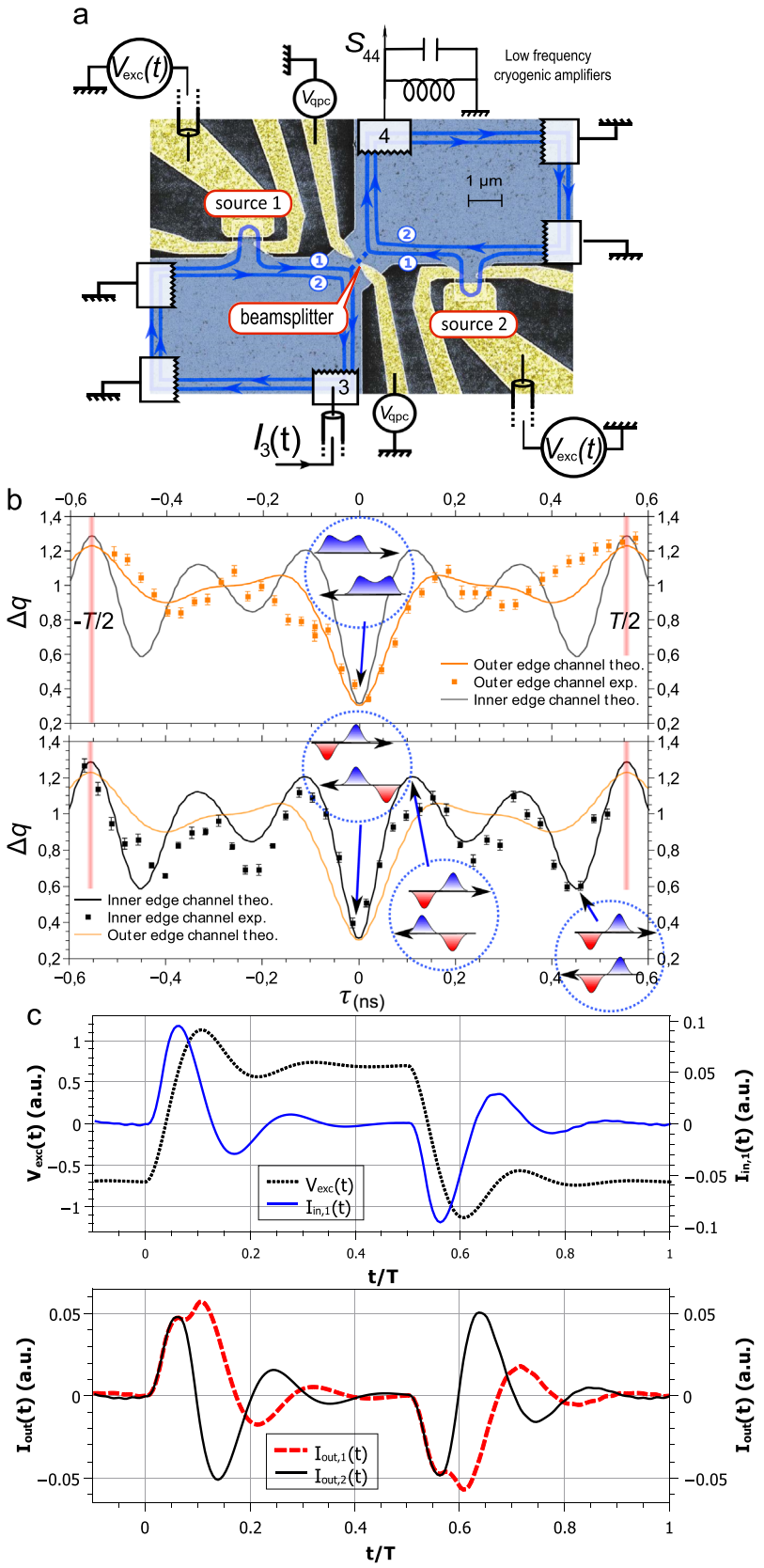

Fig. 13. (a) Modified scanning electron microscope picture of the sample. The two sources generate the charge pulse synchronously. The quantum point contact is set to partition either the outer channel (1) or the inner channel (2). The low frequency partition noise is measured on output 4. (b) Noise measurements (normalized by the random partition noise) Δq as a function of the time delay τ between the sources. The upper/lower panel represents measurements of the outer (1)/inner (2) channels. The sketches represent the shape of the current pulses colliding synchronously for the different values of delay τ. (c) Simulations of the excitation voltage and input current $I_1(x = 0, t)$ (upper panel) and of the output currents $I_1(x = l, t)$ and $I_2(x = l, t)$.

seen in the previous section, the propagation of currents obeys coupled equations in which eigenmodes involve charge excitations on both channels. As a result, at the output of the interaction region, charge excitations have been created in channel 2 and the charge Q in channel 1 has fractionalized in several packets. The two situations corresponding to interactions between copropagating channels (situation 1) or between counterpropagating channels (situation 2) are depicted in Fig. 12 on panels a and b.

In situation 1, the charge initially emitted in channel 1 decomposes on the symmetric charge mode and antisymmetric neutral mode. As these two eigenmodes travel at different velocities, the pulse of charge Q fractionalizes in two pulses of charge $Q/2$ in channel 1. A dipolar excitation consisting in two pulses of charge $Q/2$ and $-Q/2$ is left in channel 2. In situation 2, the propagating eigenmode consists in the charge Q in channel 1 dragging charge $-rQ$ in channel 2, such that the total charge $(1-r)Q$ propagates along the coupled channels. Due to charge conservation in channel 2, a charge rQ is reflected in channel 2 when the charge Q in channel 1 enters the interaction region.

As can be seen in the sketches of Fig. 12, the observation of charge fractionalization calls for time resolved measurements of the currents flowing in each edge channel. Below the sketches representing each situation, a trace of the currents at the input, $I_1(x=0,t)$ (black line), and output, $I_1(x=l,t)$ (red dashed dotted line) and $I_2(x=l,t)$ (blue dashed line), of the interaction region is plotted in Fig. 12. The current traces result from simulations using the input/ouptut relations for each situation. In situation 1, the traces reproduce the above qualitative discussion: two pulses of same sign are observed on output 1 while two pulses of opposite sign are observed on output 2. In situation 2, a pulse rQ is observed in channel 2 simultaneously as the entrance of pulse Q in channel 1 in the interaction region. A succession of pulses is observed at later times in both channels, they result from successive reflections of the pulses at the output of the interaction region (the time delay between two pulses in one channel corresponds to $2l/|v_\pm|$). The time unit in Fig. 12 is arbitrary but an estimate of the time resolution needed to observe the splitting of charge in successive pulses can be obtained using a typical length $l \approx 10$ μm and a typical velocity $v \approx 10^5$ m s^{-1} giving a time resolution better than $\tau \approx 100$ ps.

Situation 2 has been experimentally investigated in Ref. [65] by generating a current pulse of charge $Q \approx 150$ e and duration ≈500 ps and measuring the time dependent current resulting from the fractionalization process. A time resolution of a few tens of picoseconds was obtained by varying on a short time the transmission of a quantum point contact placed at the output of the interaction region. This allowed us to sample the current as a function of the delay between the injection of the incoming charge pulse and the closing of the output QPC. The technique could accurately measure the reflected charge pulse on channel 2 at the input of the interaction region providing $r \approx 0.04$ and the velocity of the eigenmodes in the interaction region $v_\pm \approx 1.5 \times 10^5$ m s^{-1}. Both values are in agreement with calculations of the involved capacitances and the predictions of Eqs. (57) and (54).

In Ref. [69], we investigated charge fictionalization in situation 1 by generating a current pulse in channel 1 using a mesoscopic capacitor on which we applied a step voltage. The pulse carries charge $Q \approx e$ and its duration $\tau \approx 40$ ps is limited by the risetime of the excitation pulse. The sample is identical to the one presented in Fig. 7 but the excitation voltage differs: instead of a sine excitation of variable frequency, a periodic step voltage of frequency $f = 0.9$ GHz (period T) is applied on the metallic top gate of the quantum dot. Note that the charge carried by the pulse is very close to the elementary electric charge, however in this experiment, the quantum dot is perfectly coupled to edge channel number 1 (outer edge) such that the emitted charge is not quantized and does not correspond to single electron emission. Time domain information on the output current is obtained not by measuring directly the current but by performing the electronic analog [31,32] of the Hong-Ou-Mandel [70] (HOM) experiment at the output of the interaction region. It requires two sources placed at the input of a quantum point contact (see Fig. 13a). When indistinguishable particles collide on the beam-splitter, two-particle interference effects related to quantum exchange occur [71–73] and show up in the fluctuations of the number of particles counted at the output (noise). The output current noise thus measures the degree of indistinguishability of the states incoming at the input of the splitter. As in the seminal HOM experiment, two-particle interference effects can be used to acquire short time information on the shape of the current pulses at the input : it provided the length of a single photon wavepacket with a subpicosecond time resolution in the original experiment, we use it to unveil the fractionalization in two charge pulses [74] with a resolution of ten picoseconds in our case. In order to generate a charge pulse at each input of the QPC, the quantum dot placed in input 2 (source 2 in Fig. 13a) is also time dependently driven by a step voltage in order to generate a pulse identical to the one generated by source 1.

Interestingly, HOM interferometry can be performed on both channels 1 and 2 by setting the QPC to partition either channel 1 or channel 2, so as to recover information on the current traces on these two channels. The resulting noise measurements as a function of the time delay τ between the sources are presented in Fig. 13b. The upper/lower traces represent the outer (1)/inner (2) channels partitioning measurements. On both traces a dip in the noise can be seen at $\tau \approx 0$ resulting from the antibunching between undistinguishable pulses when the sources are perfectly synchronized. Importantly the dip width observed on channel 1 when the time delay is increased is twice larger than the one observed on channel 2 (80 ps compared to 40 ps). This increased width results from the splitting of the charge pulse in channel 1 in two separate pulses (see sketch in Fig. 13b, upper panel). As the time separation $\tau_s \approx l/v_n \approx 70$ ps is comparable with the pulse width ≈40 ps, the separation is not complete but results in an increase of the pulse width which matches the separation time. On channel 2 the dip at $\tau = 0$ evolves to a small peak in the noise for $\tau \approx \tau_s = 70$ ps revealing the collision between charges of opposite signs (electron vs holes) [75]. This shows the dipolar nature of the current pulse in channel 2 as a result of the interchannel interaction (see sketch in Fig. 13b, lower panel). On long time delay $\tau \approx T/2$, the noise shows a peak on channel 1 which results, as stated before, from collisions between electrons and holes. This behavior is expected as, the dot being ac coupled, emission of an electron type pulse at time $t \approx 0$ is followed by the emission of a hole one at time $t \approx T/2$. The noise trace is completely different on channel 2. A peak is also observed for $\tau = T/2$ (for the same reason as mentioned before) but a dip is observed for $\tau \approx T/2 - \tau_s$ which is not present on channel 1. It signals an electron-electron type collision which results from the fractionalization process: due to the dipolar nature of the current on channel 2, collisions between charges of the same sign occur at $\tau \approx T/2 - \tau_s$.

These results are nicely reproduced by the propagation model presented in the previous section, taking the input pulse represented in Fig. 13c (upper panel). The simulations of the currents at the output of the interaction region are represented on the lower panel Fig. 13c resulting from the calculations of Eq. (45) with $\tau_s = 70$ ps. As discussed before, the two pulses on channel 1 are not fully separated and the current trace on channel 2 has a dipolar form. The input current pulse shows a rebound at $\tau \approx 150$ ps resulting from the rebound included on the excitation voltage pulse (black dashed line upper panel). This rebound has to obtain a good quantitative agreement between the noise data and the simulations (red and black lines) in Fig. 13b. In particular, the additional

dip observed on the noise traces for channel 1 ($\tau \approx \pm 400$ ps and channel 2 ($\tau \approx \pm 250$ ps) are only reproduced when adding this rebound.

7. Chiral Luttinger liquid description and single electron fractionalization

As seen in the previous sections, Coulomb interaction effects play a major role in the transport along chiral quantum Hall edge channels. As seen in Sections 2, 3 and 4 at low frequency, they are encoded in the electrochemical capacitances in a lumped element description of the circuit, which behavior can be either inductive or capacitive depending on its geometry. At higher frequencies, propagation effects need to be taken into account and the lumped element description breaks down. Propagation is then described in terms of a velocity matrix describing the coupling between the edge channels. As seen in Sections 5 and 6, Coulomb interaction determines the nature of the propagating eigenmodes and their velocity (related to the above-mentioned electrochemical capacitances).

At this point, the coherence of the electronic wavefunction and its effect on electronic propagation has not been discussed as single electron interference effects were not considered. These interferences between multiple paths can be introduced in a scattering matrix description of time dependent electronic transport developed by M. Büttiker and his collaborators in various works [2,4]. The purpose of this final section is not to introduce these interference effects but to discuss how electronic coherence on which they rely is affected by Coulomb interaction. To address this question, we will consider the simple case of a single electron propagating in the conductor. As we will see, it differs strongly from the propagation of a classical pulse discussed in the previous section. This single electron state with wavefunction $\phi_e(x)$ propagating above the Fermi energy of the edge channel k can be written in the following way:

$$|\Psi_k\rangle = \int dt \phi_e(x) \Psi_k^\dagger(x) |F_k\rangle \tag{58}$$

where $\Psi_k^\dagger(x)$ creates an electron at position x of the edge channel k, on top of the fermi sea represented by the many-body state $|F_k\rangle$.

The sketch depicted in Fig. 12a representing charge fractionalization in the $N=2$ case provides an insight on how Coulomb interaction affects single electron propagation. The single electron is emitted on channel 1, the blue pulse now representing the wavepacket $\phi_e(x)$. As the electron enters the interaction region, it fractionalizes in two distinct pulses, exactly as in the classical case studied in the previous section. However, the consequences are much more drastic. Indeed, once the fractionalization process has taken place, the pulses carrying charge $e/2$ cannot obviously be described as single electron states, meaning that they involve numerous electron/hole excitations of the Fermi sea which total charge matches half the electron charge. The fractionalization process thus leads to the creation of collective excitations (electron/hole pairs) in which the originally emitted electron dilutes. In the process, collective excitations are also created in channel 2 which was originally empty. The energetic cost associated with the creation of these collective excitations is associated with the energy relaxation of the electron [51,55], it also leads to the decoherence [69,74,76,77] of the single electron wavepacket.

To go beyond this simple picture, one needs to include Coulomb interaction effects in the single electron dynamics, which, in general, is not a simple task. Here because of the specific one dimensional nature of the problem, the full interaction problem can be solved in terms of the propagation of bosonic modes [78] which are nothing but the edge magnetoplasmon modes considered in the two previous sections. In this bosonic description, a bosonic field $\hat{\phi}_k(x, t)$ is introduced for each chiral edge channel. It is related to the charge density $\hat{\rho}_k(x, t)$ by $\hat{\rho}_k(x, t) = -(e/\sqrt{\pi})\partial_x\hat{\phi}_k(x, t)$ and to the electrical current by $\hat{i}_k(x, t) = (e/\sqrt{\pi})\partial_t\hat{\phi}_k(x, t)$ (from the charge conservation equation). The dynamics of the bosonic field is described with the chiral Luttinger liquid theory [79,80] which Hamiltonian is the sum of the free motion plus the long range Coulomb interaction between the charge densities of the various channels [54]:

$$H = \sum_k \hbar v_{D,k} \int dx \left(\partial_x\hat{\phi}_k(x, t)\right)^2 + \frac{e^2}{2\pi}\sum_{k,j}\int dy\, dx \partial_x\hat{\phi}_k(x, t) U_{kj}(x, y)\partial_x\hat{\phi}_j(y, t) \tag{59}$$

From Eq. (59), we can deduce the equation of motion of the field $\hat{\phi}_k(x, t)$ and of the current $\hat{i}_k(x, t)$:

$$(\partial_t + v_{D,k}\partial_x)\hat{\phi}_k(x, t) = \frac{e\sqrt{\pi}}{h} U_k(x, t) \tag{60}$$

$$U_k(x, t) = \sum_j \int dy U_{kj}(x, y)\partial_x\hat{\rho}_j(x, t) \tag{61}$$

$$(\partial_t + v_{D,k}\partial_x)\hat{i}_k(x, t) = \frac{e^2}{h}\partial_t U_k(x, t) \tag{62}$$

Eq. (62) for the current operator is the exact analog of the classical calculation of the current made in Section 5, see Eq. (36).

As in Section 5, solutions are easier to express at a given pulsation ω using the Fourier decomposition of the field and the current:

$$\hat{\phi}_k(x, t) = -\frac{i}{\sqrt{4\pi}}\int \frac{d\omega}{\sqrt{\omega}}\hat{b}_k(\omega)e^{i\omega(x/v_{D,k}-t)} - h.c. \tag{63}$$

$$\hat{i}_k(x, t) = -e\int \frac{d\omega}{2\pi}\sqrt{\omega}\hat{b}_k(\omega)e^{i(x/v_{D,k}-t)} + h.c. \tag{64}$$

where $\hat{b}_k(\omega)$ annihilates a single boson (plasmon) at energy $\hbar\omega$ in edge channel k. Using the work developed in the previous sections, the solutions of the propagation equations for $\hat{\phi}_k$ and $\hat{i}_k$ are already known. Once the eignemodes of the velocity matrix have been found, one can compute the scattering matrix $S(\omega, l)$ relating the field at pulsation ω at the output of the interaction region ($x=l$) to the field at the input ($x=0$):

$$\Phi(\omega, x = l) = S(\omega, l)\Phi(\omega, x = 0) \tag{65}$$

where Φ is the vector of the ω component of the field on all the edge channels. Finally, the connection to the original electronic problem is made through the bosonization procedure relating the fermionic field to the bosonic one [78]:

$$\Psi_k^\dagger(x) = \frac{U_k^\dagger}{\sqrt{2\pi a}} e^{-i\sqrt{4\pi}\phi_k(x)} \tag{66}$$

where a is a short distance cutoff and $U_k^\dagger$ a Klein factor which ensures fermionic anticommutation relations. This provides a straightforward route to calculate the evolution of the single electron state when it goes through the interaction region. Firstly one solves the dynamics of the coupled bosonic fields $\phi_k(x, t)$ by finding the eigenmodes of propagation from which the coefficients of the scattering matrix are deduced. One then computes the electron state at the output of the interaction region using Eqs.

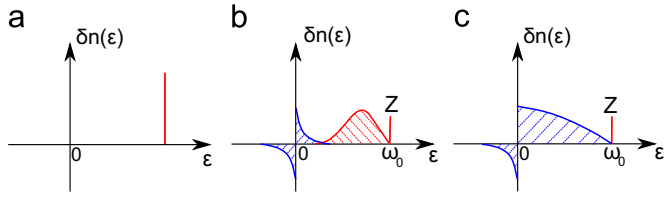

Fig. 14. (a) Sketch of the energy distribution of emitted particles at the input of the interaction region. An electron is incoming at a well defined energy $\hbar\omega_0$ represented by a quasiparticle peak. (b) Sketch of the energy distribution at the output of the interaction region in the weak coupling case. The quasiparticle peak is reduced to height $Z(\omega_0)$, a relaxation tail emerges (red line) and electron/hole pairs (blue line) are created at the Fermi surface. (c) Sketch of the energy distribution at the output of the interaction region in the strong coupling case. The relaxation tail merges with the created electron/hole pairs and cannot be distinguished from it. (For interpretation of the references to color in this figure caption, the reader is referred to the web version of this paper.)

(65) and (66).

Before dealing with the single electron case, let us first compute the evolution of a classical charge pulse discussed in section 6 within this formalism (situations 1 and 2 discussed in the previous section). In the bosonic description, a classical sinusoidal pulse at pulsation ω is represented as a quasi-classical or coherent state, that is, an eigenstate $|-\frac{1}{e\sqrt{\omega}}I(\omega)\rangle$ of the annihilations operator $\hat{b}(\omega)$: $\hat{b}(\omega)|-\frac{1}{e\sqrt{\omega}}I(\omega)\rangle = -\frac{I(\omega)}{e\sqrt{\omega}}|-\frac{1}{e\sqrt{\omega}}I(\omega)\rangle$. The state of a generic classical pulse and the corresponding average electrical current $i(x,t)$ are then deduced by summing on all the pulsations:

$$|\Psi_{class}\rangle = \otimes_{\omega>0}\,|-\frac{1}{e\sqrt{\omega}}I(\omega)\rangle \tag{67}$$

$$i(x,t) = \langle\hat{i}(x,t)\rangle = \int\frac{d\omega}{2\pi}I(\omega)e^{i(x/v_{D,k}-t)} + h.c., \tag{68}$$

and $I(\omega)$ finally appears to be the Fourier component at pulsation ω of the classical current pulse $i(x,t)$. These coherent states are naturally generated when an edge channel is driven by a classical time dependent voltage drive $V(t)$ of Fourier component $V(\omega)$, with $I(\omega) = (e^2/h)V(\omega)$. In situation 1 for example, at the input of the interaction region, $x=0$, edge channel 1 is driven by a classical drive $V(t)$ whereas edge channel 2 (which plays the role of an environment for channel 1) is in the ground state described by the vacuum (zero temperature is assumed):

$$|\Psi_{in}\rangle = \otimes_{\omega>0}\left|-\frac{e}{h\sqrt{\omega}}V(\omega)\right\rangle_1 \otimes |0\rangle_{env} \tag{69}$$

Using the scattering matrix $S(\omega,l)$ and Eq. (65), the effect of Coulomb interaction on the quasiclassical states of the bosonic description can be easily computed. The state at the output of the interaction region then reads

$$|\Psi_{out}\rangle = \otimes_{\omega>0}\left[\left|-S_{11}\frac{e}{h\sqrt{\omega}}V(\omega)\right\rangle_1 \otimes \left|-S_{21}\frac{e}{h\sqrt{\omega}}V(\omega)\right\rangle_{env}\right] \tag{70}$$

The output state is still described as a product of coherent states. It is entirely determined by the currents flowing in each conductor resulting from the edge magnetoplasmon scattering. For example, considering the $N=2$ case, everything happens as if the edge channels were not interacting but channel 1 was driven by the voltage $S_{11}(\omega)V(\omega)$ and channel 2 by $S_{21}(\omega)V(\omega)$. In particular, once the fractionalization process has fully taken place and the input pulse has split into two separate pulses, nothing particular can be seen on the bosonic description of the output state. Everything happens as if the excitation voltage of channel 1 consisted in two successive pulses. As studied by Degiovanni and coworkers in Refs. [76,77,28], the situation is completely different in the single electron case. Using Eqs. (58) and (67), the single electron state at the input and output of the interaction region can be expressed in the bosonic description:

$$|\Psi_{in}\rangle = \int dx\phi_e(x)\otimes_{\omega>0}\left[\left|-\frac{e^{i\frac{\omega}{v_D}x}}{\sqrt{\omega}}\right\rangle_1 \otimes |0\rangle_{env}\right] \tag{71}$$

$$|\Psi_{out}\rangle = \int dx\phi_e(x)\otimes_{\omega>0}\left[\left|-S_{11}\frac{e^{i\frac{\omega}{v_D}x}}{\sqrt{\omega}}\right\rangle_1 \otimes \left|-S_{21}\frac{e^{i\frac{\omega}{v_D}x}}{\sqrt{\omega}}\right\rangle_{env}\right] \tag{72}$$

Compared to the classical case, the input state is now described as a coherent superposition of quasi-classical states, each component of the wavefunction $\phi_e(x)$ giving rise to a different plasmonic coherent state. Each of these x dependent coherent states is scattered in the interaction region. As a result, the output state is an entangled state between the edge channel and the other Coulomb interacting conductors. Tracing out the environment degrees of freedom, this x dependent scattering leads to a decoherence factor between two components x_+ and x_- of the electronic wavepacket:

$$D_{ext}(x_+,x_-) = \otimes_{\omega>0}\ {}_{env}\left\langle -S_{21}\frac{e^{i\frac{\omega}{v_D}x_+}}{\sqrt{\omega}}|-S_{21}\frac{e^{i\frac{\omega}{v_D}x_-}}{\sqrt{\omega}}\right\rangle_{env} \tag{73}$$

$$= e^{\int_0^{+\infty}\frac{d\omega}{\omega}|S_{21}(\omega)|^2\left(e^{-i\frac{\omega(x_+-x_-)}{v_D}}-1\right)} \tag{74}$$

The extrinsic decoherence factor is not the only contribution to decoherence. Indeed, the remaining state in channel 1 does not correspond anymore to a single electron above the Fermi sea due to the ω dependence of the scattering coefficient $S_{11}(\omega)$. In addition to the initially emitted electron, additional electron/hole pairs have been created in the interaction process leading to the relaxation of the single electron energy. This decoherence scenario is illustrated in Fig. 14 on the example of an electron emitted at the input of the interaction region at a well defined energy $\epsilon_0 = \hbar\omega_0$ above the Fermi sea. The energy distribution in channel 1 at the input of the interaction region is represented on the sketch of Fig. 14a). It consists of a single peak at energy $\hbar\omega_0$ as the contribution of the Fermi sea has been subtracted. At the output of the interaction region, two possibilities have to be considered. The weak interaction case is depicted by the sketch of Fig. 14b: the relaxation of energy of the electron leads to the appearance of a relaxation tail for $\epsilon \le \epsilon_0$ and a decrease of the quasiparticle peak at ϵ_0. Electron/hole pairs are also created close to the Fermi sea. As can be seen in Fig. 14b, the electron contribution can still be distinguished from the additional electron/hole pairs created close to the Fermi surface. In this case, an effective density matrix [76,81] can be written to describe the single electron state at the output of the interaction region:

$$\rho_{out}(x_+,x_-) = \phi_e(x_+)\phi_e(x_-)^* D_{tot}(x_+,x_-) \tag{75}$$

$$D_{tot}(x_+,x_-) = e^{\int_0^{+\infty}\frac{d\omega}{\omega}2\,Re\left(1-S_{11}(\omega)\right)\left(e^{-i\frac{\omega(x_+-x_-)}{v_D}}-1\right)} \tag{76}$$

Compared to Eq. (74), an additional contribution has been added to the extrinsic decoherence factor. This additional coefficient accounts for the loss of coherence associated with the creation of the additional electron hole/pairs. Note that the full decoherence factor (or even the full many-body state) is expressed as a function of the plasmon scattering parameters $S_{11}(\omega)$ and $S_{21}(\omega)$ which are themselves directly related to the high frequency conductance

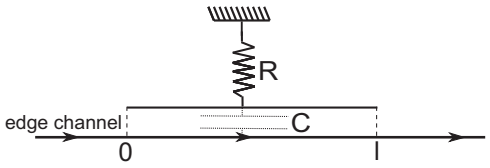

Fig. 15. Sketch of the capacitive coupling of an edge channel to a resistive conductor.

measurements as seen in Section 5. As an example of the connection between high frequency conductance and decoherence, we can consider the case where edge channel (1) is coupled with a capacitance C to a metallic conductor with resistance $R \ll R_K$. In this limit considered in Refs. [82,76] the low frequency description of the circuit fully encodes the single electron relaxation. In particular, the elastic scattering probability Z_{ω_0}, which is the height of the quasiparticle peak after interaction can be directly related to the lumped element description of the circuit: $Z(\omega_0) = 1 - R/R_K(R_K C_\mu \omega_0)^2$ (Fig. 15).

However, it is not always possible to separate the initially emitted electron from the electron/hole pairs created in the interaction process. This situation is described by the sketch of Fig. 14c: the relaxation tail fully merges with the electron/hole excitation of the Fermi surface. One has then to rely on the full expression of the output many-body state. It is the case in particular at $N=2$ in the regime of strong coupling between copropagating edge channels, where as seen in Section 5, $S_{21}(\omega)$ is close to one in a very large range of frequencies. Single electron decoherence and relaxation have then to be numerically calculated [74,77] starting from the knowledge of the scattering parameters S_{21} and S_{11} extracted from the high frequency conductance measurements. As seen in Refs. [74,77] before the full fractionalization of the charge in two distinct pulses, the electron energy relaxes close to the Fermi surface and the coherence is strongly suppressed

8. Conclusion

We have investigated time dependent electronic transport along the chiral edge channels of the quantum Hall regime, and in particular, the role of Coulomb interaction. At low frequency, a lumped element description of the circuit can be used to model the ac conductance $G(\omega)$. Depending on the geometry of the circuit, the ac response is capacitive or inductive, the capacitance and inductance being related to the electrochemical capacitances in the circuit. They are given by the serial association of the quantum capacitance related to the non-interacting density of states in the conductor and the geometrical capacitance which encodes Coulomb interaction. At higher frequency, propagation effects need to be taken into account by solving the propagation equation of the Coulomb coupled edge channels. The propagation eigenmodes correspond to a charge distributed on all the edge channels. As a consequence, a charge pulse emitted in a given edge fractionalizes on several pulses. Finally, Coulomb interaction can be conveniently described in a chiral Luttinger liquid description of the coupled channels. It describes Coulomb interaction as the propagation and scattering of collective bosonic excitations (plasmons) in the coupled conductors. Using the bosonization technique, one can then study the effects of Coulomb interaction, and in particular, the consequences of the charge fractionalization process, on a single electron state. As the single electron wavepacket splits in distinct pulses, the single electron energy relaxes down to the Fermi level and the single electron coherence is suppressed. The preservation of single electron coherence thus requires the implementation of schemes to reduce or suppress interaction induced decoherence.

Acknowledgments

We want to thank all the people who have been involved in the work presented in this paper during the past years: D.C. Glattli, Y. Jin, A. Cavanna, B. Etienne, P. Degiovanni, J. Gabelli, A. Mahé, F.D. Parmentier, E. Bocquillon, V. Freulon and A. Marguerite.

References

[1] M. Büttiker, H. Thomas, A. Prêtre, Mesoscopic capacitors, Phys. Lett. A 180 (1993) 364.
[2] M. Büttiker, A. Prêtre, H. Thomas, Dynamic conductance and the scattering matrix of small conductors, Phys. Rev. Lett. 70 (1993) 4114.
[3] M. Büttiker, Capacitance, admittance, and rectification properties of small conductors, J. Phys.: Condens. Matter 5 (1993) 9361.
[4] A. Prêtre, H. Thomas, M. Büttiker, Dynamic admittance of mesoscopic conductors: discrete-potential model, Phys. Rev. B 54 (1996) 8130.
[5] M. Büttiker, Y. Imry, R. Landauer, S. Pinhas, Generalized many-channel conductance formula with application to small rings, Phys. Rev. B 31 (1985) 6207.
[6] S.E. Nigg, M. Büttiker, Quantum to classical transition of the charge relaxation resistance of a mesoscopic capacitor, Phys. Rev. B 77 (2008) 085312.
[7] J. Gabelli, G. Fève, J.-M. Berroir, B. Plaçais, A. Cavanna, B. Violation of Kirchhoff's laws for a coherent RC circuit, Science 313 (2006) 499–502.
[8] S.E. Nigg, R. Lopez, M. Büttiker, Mesoscopic charge relaxation, Phys. Rev. Lett. 97 (2006) 206804.
[9] Y. Hamamoto, T. Jonckheere, T. Kato, T. Martin, Dynamic response of a mesoscopic capacitor in the presence of strong electron interactions, Phys. Rev. B 81 (2010) 153305.
[10] C. Mora, K.L. Hur, Universal resistances of the quantum RC circuit, Nat. Phys. 6 (2010) 697.
[11] M. Büttiker, A.M. Martin, Charge relaxation and dephasing in Coulomb-coupled conductors, Phys. Rev. B 61 (2000) 2737.
[12] G. Seelig, M. Büttiker, Charge-fluctuation-induced dephasing in a gated mesoscopic interferometer, Phys. Rev. B 64 (2001) 245313.
[13] V.S.-W. Chung, P. Samuelsson, M. Büttiker, Visibility of current and shot noise in electrical Mach–Zehnder and Hanbury Brown Twiss interferometers, Phys. Rev. B 72 (2005) 125320.
[14] S. Pilgram, M. Büttiker, Efficiency of mesoscopic detectors, Phys. Rev. Lett. 89 (2002) 200401.
[15] A.A. Clerk, S.M. Girvin, A.D. Stone, Quantum-limited measurement and information in mesoscopic detectors, Phys. Rev. B 67 (2003) 165324.
[16] Y. Ji, Y. Chung, D. Sprinzak, M. Heiblum, D. Mahalu, H. Shtrikman, An electronic Mach–Zehnder interferometer, Nature 422 (2003) 415.
[17] E. Bocquillon, V. Freulon, F.D. Parmentier, J.-M. Berroir, B. Plaçais, C. Wahl, J. Rech, T. Jonckheere, T. Martin, Ch. Grenier, D. Ferraro, P. Degiovanni, G. Fève, Electron quantum optics in ballistic chiral conductors, Ann. Phys. 526 (2014) 1–30.
[18] G. Fève, A. Mahé, J.-M. Berroir, T. Kontos, B. Plaçais, D.C. Glattli, A. Cavanna, B. Etienne, Y. Jin, An on-demand coherent single-electron source, Science 316 (2007) 1169–1172.
[19] M. Moskalets, P. Samuelsson, M. Büttiker, Quantized dynamics of a coherent capacitor, Phys. Rev. Lett. 100 (2008) 086601.
[20] M. Moskalets, G. Haack, M. Büttiker, Single-electron source: adiabatic versus nonadiabatic emission, Phys. Rev. B 87 (2013) 125429.
[21] A. Mahé, F.D. Parmentier, E. Bocquillon, J.-M. Berroir, D.C. Glattli, T. Kontos, B. Plaçais, G. Fève, A. Cavanna, Y. Jin, Current correlations of an on-demand single-electron emitter, Phys. Rev. B 82 (2010) 201309.
[22] M. Albert, C. Flindt, M. Büttiker, Accuracy of the quantum capacitor as a single-electron source, Phys. Rev. B 82 (2010) 041407.
[23] T. Jonckheere, T. Stoll, J. Rech, T. Martin, Real-time simulation of finite-frequency noise from a single-electron emitter, Phys. Rev. B 85 (2012) 045321.
[24] M. Moskalets, Noise of a single-electron emitter, Phys. Rev. B 88 (2013) 035433.
[25] M. Albert, C. Flindt, M. Büttiker, Distributions of waiting times of dynamic single-electron emitters, Phys. Rev. Lett. 107 (2011) 086805.
[26] M. Albert, G. Haack, C. Flindt, M. Büttiker, Electron waiting times in mesoscopic conductors, Phys. Rev. Lett. 108 (2012) 186806.
[27] D. Dasenbrook, C. Flindt, M. Büttiker, Floquet theory of electron waiting times in quantum-coherent conductors, Phys. Rev. Lett. 112 (2014) 146801.
[28] C. Grenier, R. Herve, E. Bocquillon, F.D. Parmentier, B. Plaçais, J.M. Berroir, G. Fève, P. Degiovanni, Single-electron quantum tomography in quantum Hall edge channels, New J. Phys. 13 (2011) 093007.
[29] G. Haack, M. Moskalets, J. Splettstoesser, Markus. Büttiker, Coherence of single-electron sources from Mach–Zehnder interferometry, Phys. Rev. B 84 (2011) 081303(R).

[30] E. Bocquillon, F.D. Parmentier, C. Grenier, J.-M. Berroir, P. Degiovanni, D. C. Glattli, B. Plaçais, A. Cavanna, Y. Jin, G. Fève, Electron quantum optics: partitioning electrons one by one, Phys. Rev. Lett. 108 (2012) 196803.
[31] E. Bocquillon, V. Freulon, J.-M. Berroir, P. Degiovanni, B. Plaçais, A. Cavanna, Y. Jin, G. Fève, Coherence and indistinguishability of single electrons emitted by independent sources, Science 339 (2013) 1054–1057.
[32] S. Ol'khovskaya, J. Splettstoesser, M. Moskalets, M. Büttiker, Shot noise of a mesoscopic two-particle collider, Phys. Rev. Lett. 101 (2008) 166802.
[33] P. Samuelssonn, M. Büttiker, Dynamic generation of orbital quasiparticle entanglement in mesoscopic conductors, Phys. Rev. B 71 (2005) 245317.
[34] J. Splettstoesser, M. Moskalets, M. Büttiker, Two-particle nonlocal Aharonov–Bohm effect from two single-particle emitters, Phys. Rev. Lett. 103 (2009) 076804.
[35] G. Rossello, F. Battista, M. Moskalets, J. Splettstoesser, Interference and multiparticle effects in a Mach–Zehnder interferometer with single-particle sources, Phys. Rev. B 91 (2015) 115438.
[36] F.D. Parmentier, E. Bocquillon, J.-M. Berroir, D.C. Glattli, B. Plaçais, G. Fève, M. Albert, C. Flindt, M. Büttiker, Current noise spectrum of a single-particle emitter: theory and experiment, Phys. Rev. B 85 (2012) 165438.
[37] M. Moskalets, M. Büttiker, Floquet scattering theory of quantum pumps, Phys. Rev. B 66 (2002) 205320.
[38] M. Moskalets, Scattering Matrix Approach to Non-Stationary Quantum Transport, Imperial College Press, London, 2011.
[39] T. Christen, M. Büttiker, Low-frequency admittance of quantized Hall conductors, Phys. Rev. B 53 (1996) 2064–2072.
[40] B.I. Halperin, Quantized Hall conductance, current-carrying edge states, and the existence of extended states in a two-dimensional disordered potential, Phys. Rev. B 25 (1982) 2185.
[41] M. Büttiker, Absence of backscattering in the quantum Hall effect in multiprobe conductors, Phys. Rev. B 38 (1988) 9375.
[42] B.J. van Wees, L.P. Kouwenhoven, E.M.M. Willems, C.J.P.M. Harmans, J.E. Mooij, H. van Houten, C.W.J. Beenakker, J.G. Williamson, C.T. Foxon, Quantum ballistic and adiabatic electron transport studied with quantum point contacts, Phys. Rev. B 43 (1991) 12431.
[43] D.B. Chklovskii, B.I. Shklovskii, L.I. Glazman, Electrostatics of edge channels, Phys. Rev. B 46 (1992) 4026.
[44] P.J. Burke, Luttinger liquid theory as a model of the Gigahertz electrical properties of carbon nanotubes, IEEE Trans. Nanotechnol. 1 (2002) 129.
[45] P.J. Burke, An RF circuit model for carbon nanotubes, IEEE Trans. Nanotechnol. 2 (2003) 55.
[46] J. Gabelli, G. Fève, T. Kontos, J.-M. Berroir, B. Plaçais, D.C. Glattli, B. Etienne, Y. Jin, M. Büttiker, Relaxation time of a chiral quantum RL circuit, Phys. Rev. Lett. 98 (2007) 166806.
[47] G. Sukhodub, F. Hohls, R. Haug, Observation of an interedge magnetoplasmon mode in a degenerate two-dimensional electron gas, Phys. Rev. Lett. 93 (2004) 196801.
[48] N. Kumada, H. Kamata, T. Fujisawa, Edge magnetoplasmon transport in gated and ungated quantum Hall systems, Phys. Rev. B 84 (2011) 045314.
[49] M. Hashisaka, K. Washio, H. Kamata, K. Muraki, T. Fujisawa, Distributed electrochemical capacitance evidenced in high-frequency admittance measurements on a quantum Hall device, Phys. Rev. B 85 (2012) 155424.
[50] C. Altimiras, H. le Sueur, U. Gennser, A. Cavanna, D. Mailly, F. Pierre, Nonequilibrium edge-channel spectroscopy in the integer quantum Hall regime, Nat. Phys. 6 (2009) 34–39.
[51] H. le Sueur, C. Altimiras, U. Gennser, A. Cavanna, D. Mailly, F. Pierre, Energy relaxation in the integer quantum Hall regime, Phys. Rev. Lett. 105 (2010) 056803.
[52] P. Roulleau, F. Portier, P. Roche, A. Cavanna, G. Faini, U. Gennser, D. Mailly, Direct measurement of the coherence length of edge states in the integer quantum Hall regime, Phys. Rev. Lett. 100 (2008) 126802.
[53] P.-A. Huynh, F. Portier, H. le Sueur, G. Faini, U. Gennser, D. Mailly, F. Pierre, W. Wegscheider, P. Roche, Quantum coherence engineering in the integer quantum Hall regime, Phys. Rev. Lett. 108 (2012) 256802.
[54] I.P. Levkivskyi, E.V. Sukhorukov, Dephasing in the electronic Mach–Zehnder interferometer at filling factor $\nu=2$, Phys. Rev. B 78 (2008) 045322.
[55] P. Degiovanni, C. Grenier, G. Fève, C. Altimiras, H. le Sueur, F. Pierre, Plasmon scattering approach to energy exchange and high-frequency noise in $\nu=2$ quantum Hall edge channels, Phys. Rev. B 81 (2010) 121302.
[56] C. Grenier, R. Hervé, G. Fève, P. Degiovanni, Electron quantum optics in quantum Hall edge channels, Mod. Phys. Lett. B 25 (2011) 1053–1073.
[57] I.P. Levkivskyi, E.V. Sukhorukov, Energy relaxation at quantum Hall edge, Phys. Rev. B 85 (2012) 075309.
[58] E. Bocquillon, V. Freulon, J.-M. Berroir, P. Degiovanni, B. Plaçais, A. Cavanna, Y. Jin, G. Fève, Separation of neutral and charge modes in one-dimensional chiral edge channels, Nat. Commun. 4 (2013) 1839.
[59] D.C. Glattli, E.Y. Andrei, G. Deville, J. Poitrenaud, F.I.B. Williams, Dynamical Hall effect in a two-dimensional classical plasma, Phys. Rev. Lett. 54 (1985) 1710.
[60] R.C. Ashoori, H.L. Stormer, L.N. Pfeiffer, K.W. Baldwin, K. West, Edge magnetoplasmons in the time domain, Phys. Rev. B 45 (1992) 3894–3897.
[61] N. Zhitenev, R. Haug, K.v. Klitzing, K. Eberl, Time resolved measurements of transport in edge channels, Phys. Rev. Lett. 71 (1993) 2292.
[62] V. Talyanskii, A. Polisski, D. Arnone, M. Pepper, C. Smith, D. Ritchie, J. Frost, G. Jones, Spectroscopy of a two-dimensional electron gas in the quantum-Hall-effect regime by use of low-frequency edge magnetoplasmons, Phys. Rev. B 46 (1992) 12427–12432.
[63] M. Hashisaka, H. Kamata, N. Kumada, K. Washio, R. Murata, K. Muraki, T. Fujisawa, Distributed-element circuit model of edge magnetoplasmon transport, Phys. Rev. B 88 (2013) 235409.
[64] I. Safi, H.J. Schulz, Interacting electrons with spin in a one-dimensional dirty wire connected to leads, Phys. Rev. B 59 (1999) 3040.
[65] H. Kamata, N. Kumada, M. Hashisaka, K. Muraki, T. Fujisawa, Fractionalized wave packets from an artificial Tomonaga–Luttinger liquid, Nat. Nanotechnol. 9 (2014) 177–181.
[66] E. Berg, Y. Oreg, E.-A. Kim, F. von Oppen, Fractional charges on an integer quantum Hall edge, Phys. Rev. Lett. 102 (2009) 236402.
[67] Ch. Grenier, J. Dubois, T. Jullien, P. Roulleau, D.C. Glattli, P. Degiovanni, Fractionalization of minimal excitations in integer quantum Hall edge channels, Phys. Rev. B 88 (2013) 085302.
[68] H. Inoue, A. Grivnin, N. Ofek, I. Neder, M. Heiblum, V. Umansky, D. Mahalu, Charge fractionalization in the integer quantum Hall effect, Phys. Rev. Lett. 112 (2014) 166801.
[69] V. Freulon, A. Marguerite, J.-M. Berroir, B. Plaçais, A. Cavanna, Y. Jin, G. Fève, Hong–Ou–Mandel experiment for temporal investigation of single-electron fractionalization, Nat. Commun. 6 (2015) 6854.
[70] C.K. Hong, Z.Y. Ou, L. Mandel, Measurement of subpicosecond time intervals between two photons by interference, Phys. Rev. Lett. 59 (18) (1987) 2044–2046.
[71] R.C. Liu, B. Odom, Y. Yamamoto, S. Tarucha, Quantum interference in electron collision, Nature 391 (1997) 263.
[72] P. Samuelsson, E.V. Sukhorukov, M. Büttiker, Two-particle Aharonov–Bohm effect and entanglement in the electronic Hanbury Brown–Twiss setup, Phys. Rev. Lett. 92 (2004) 026805.
[73] I. Neder, N. Ofek, Y. Chung, M. Heiblum, D. Mahalu, V. Umansky, Interference between two indistinguishable electrons from independent sources, Nature 448 (2007) 333.
[74] C. Wahl, J. Rech, T. Jonckheere, T. Martin, Interactions and charge fractionalized in an electronic Hong–Ou–Mandel interferometer, Phys. Rev. Lett. 112 (2014) 046802.
[75] T. Jonckheere, J. Rech, C. Wahl, T. Martin, Electron and hole Hong–Ou–Mandel interferometry, Phys. Rev. B 86 (2012) 125425.
[76] P. Degiovanni, C. Grenier, G. Fève, Decoherence and relaxation of single-electron excitations in quantum Hall edge channels, Phys. Rev. B 80 (2009) 241307(R).
[77] D. Ferraro, B. Roussel, C. Cabart, E. Thibierge, G. Fève, Ch. Grenier, P. Degiovanni, Real-time decoherence of Landau and Levitov quasiparticles in quantum Hall edge channels, Phys. Rev. Lett. 113 (2014) 166403.
[78] J. von Delft, H. Schoeller, Bosonization for beginners-refermionization for experts, Ann. Phys. 7 (1998) 225.
[79] X.G. Wen, Chiral Luttinger liquid and the edge excitations in the fractional quantum Hall states, Phys. Rev. B 41 (1990) 12838.
[80] A.M. Chang, Chiral Luttinger liquids at the fractional quantum Hall edge, Rev. Mod. Phys. 75 (2003) 1449.
[81] C. Grenier, Electronic quantum optics (Ph.D. thesis), tel-00617869, June 2011.
[82] G. Feve, P. Degiovanni, T. Jolicoeur, Quantum detection of electronic flying qubits in the integer quantum Hall regime, Phys. Rev. B 77 (2008) 035308.